

ATMOSPHERIC TURBULENCE CHARACTERIZATION  
OF A LOW ALTITUDE LONG  
HORIZONTAL PATH

THESIS

Presented to  
the Graduate Faculty of the  
School of Engineering  
UNIVERSITY OF DAYTON

In Partial Fulfillment of the  
Requirements for the Degree of  
Master of Science in Electro-Optics

by  
Wesley Allan Bernard

UNIVERSITY OF DAYTON

Dayton, Ohio

August 1996

UNIVERSITY OF DAYTON ROESCH LIBRARY

# Atmospheric Turbulence Characterization Of A Low Altitude Long Horizontal Path

Approved By:

Bradley D. Duncan, Ph.D.  
Assistant Professor of Electrical  
Engineering and Electro-Optics  
Chairman, Advisory Committee

Gordon Little, Ph.D.  
Assistant Professor of Electrical  
Engineering and Electro-Optics  
Member, Advisory Committee

Byron M/ Welsh, Ph.D.  
Associate Professor of Electrical  
and Computer Engineering  
Air Force Institute of Technology  
Wright Patterson AFB  
Member, Advisory Committee

Major Michael C. Roggemann, Ph.D.  
Assistant Professor of Engineering Physics  
Air Force Institute of Technology  
Wright Patterson AFB  
Member, Advisory Committee

Donald L. Moon, Ph.D.  
Associate Dean  
Graduate Engineering Programs and Research  
School of Engineering

Joseph Lestingi, D.Eng., P.E.  
Dean  
School of Engineering

## ABSTRACT

### ATMOSPHERIC TURBULENCE CHARACTERIZATION OF A LOW ALTITUDE LONG HORIZONTAL PATH

Bernard, Wesley Allan  
University of Dayton, 1996

Advisor: Dr. B. D. Duncan

The limitations placed on optical imaging through the earth's atmosphere are well understood. A large portion of the body of work on this subject deals with vertical optical paths. The transition to the study of horizontal propagation of light is currently being made. Various methods exist that quantify the disturbances introduced on optical signals by turbulent air. Small perturbations of the wave front phase can be measured using a Hartmann Wave Front Sensor (H-WFS). For long regions of turbulence, spatial and temporal variations in intensity, called scintillation, arise. Using scintillation statistics and theoretical expressions for structure functions of H-WFS slope values, turbulence strength was studied. These slope structure functions are themselves functions of the phase structure function. The Kolmogorov model of turbulence was assumed. The limitation that Kolmogorov theory applies only to vertical propagation, and the possible effects of strong scintillation on measured phase realizations were discussed. Data sets taken from two observatories in Hawaii dur-

ing an optical communications experiment were studied for comparison with slope structure function theory and scintillation statistics. This experiment was performed at an altitude of 10,000 feet over a horizontal path length of 150 km. Results indicate that the H-WFS measured very strong scintillation under these conditions, and that very little faith can be placed in the phase-dependent results. Scintillation may provide a more dependable method for optical characterization of these conditions.

## ACKNOWLEDGMENTS

Many thanks are due for the completion of this thesis. Thanks to my advisor, Dr. Brad Duncan, for his encouragement, understanding and patience while this work was conducted. Thanks also to Dr. Gordon Little for taking the time to read and comment on this work and provide a fresh perspective. Tremendous thanks goes to the United States Air Force, specifically the Air Force Institute of Technology and Wright Laboratory at Wright Patterson Air Force Base. Special thanks to Dr. Byron Welsh for his daily help and his ability to grasp problems and uncover workable solutions. Insight and support was required and readily offered by Maj. Mike Roggemann, who could always ask the right question or provide the right answer. Bob Feldmann launched the project and kept our eyes on the applicable goals. Dan Zambon provided invaluable computer support and laughter along the way. Eric Silbaugh pioneered much of the work I used in the area of slope structure functions, and was patient enough to pass it on to me. Cindy Hyde and Grant Frensley were invaluable in getting the project on its feet. And ultimate thanks goes to the Creator for providing both the subject to study and the chance to study it.

Wesley Allan Bernard

# TABLE OF CONTENTS

	Page
Abstract . . . . .	iii
Acknowledgments . . . . .	v
List of Figures . . . . .	x
List of Tables . . . . .	xii
List of Symbols . . . . .	xiii
I. Introduction . . . . .	1
1.1 Background . . . . .	1
1.2 Previous Work . . . . .	3
1.3 The Maui Experiment . . . . .	4
1.4 Problem Description And Goals . . . . .	6
1.5 Summary . . . . .	6
II. Theory . . . . .	8
2.1 Atmospheric Turbulence . . . . .	9
2.2 Structure Functions . . . . .	11
2.2.1 Phase Structure Functions . . . . .	11
2.2.2 Slope Structure Functions . . . . .	13
2.3 Scintillation . . . . .	16

	Page
III. Statistical Methods . . . . .	20
3.1 Hartmann Wave Front Sensors . . . . .	21
3.1.1 Camera Image Processing . . . . .	23
3.1.2 Computer Methods and Phase Reconstruction . . . . .	25
3.2 Slope Statistics Analysis . . . . .	27
3.2.1 Slope Structure Functions . . . . .	28
3.2.2 Homogeneity-Isotropy . . . . .	29
3.2.3 Fried Parameter . . . . .	33
3.3 Scintillation Statistics . . . . .	38
3.3.1 Correlation . . . . .	38
3.3.2 Intensity Distribution . . . . .	39
3.3.3 Fried Parameter . . . . .	41
IV. Data Analysis And Results . . . . .	42
4.1 Data Sets . . . . .	42
4.2 Slope Structure Functions . . . . .	43
4.3 Site Specifics . . . . .	48
4.4 Summary . . . . .	50
V. Conclusions . . . . .	52
5.1 Results and conclusions . . . . .	52
5.2 Further Study . . . . .	53
Appendix A. Data Set Images . . . . .	54
Appendix B. Computer Code Guide . . . . .	65
B.1 Slope Determination . . . . .	65
B.1.1 ACENTRAVG.M . . . . .	65
B.1.2 ATLCC3GB.M . . . . .	66

	Page
B.1.3 AFSLOPES.M . . . . .	66
B.1.4 ATLCC4.M . . . . .	66
B.1.5 PEAKFND3.M . . . . .	66
B.1.6 SANALYZE3.M . . . . .	66
B.1.7 R15.MAT . . . . .	66
B.1.8 VIEWER.M . . . . .	66
B.1.9 VMOVIE2.M . . . . .	67
B.2 Statistical Analysis Using Slope Values . . . . .	67
B.2.1 DSGEN.M . . . . .	67
B.2.2 DSXX.M . . . . .	67
B.2.3 DS_ARG.M . . . . .	67
B.2.4 ACEFILES.M . . . . .	67
B.2.5 ACERead.M . . . . .	67
B.2.6 ACEVIEW.M . . . . .	67
B.2.7 DSX.M . . . . .	68
B.2.8 DSY.M . . . . .	68
B.2.9 DSN45.M . . . . .	68
B.2.10 DSP45.M . . . . .	68
B.2.11 DSTRUCT.M . . . . .	68
B.2.12 DSTAR.M . . . . .	69
B.2.13 WFS_STAT.M . . . . .	69
B.2.14 DVIEW.M . . . . .	69
B.2.15 DPICK.M . . . . .	69
B.2.16 SPCAVG.M . . . . .	69
B.2.17 CORRI2.M . . . . .	70
B.2.18 CORRVIEW.M . . . . .	70
B.2.19 FITAB.M . . . . .	70



	Page
B.2.20 SFGENAB.M . . . . .	70
B.2.21 HISTT.M . . . . .	70
B.2.22 PROBI4.M . . . . .	71
B.2.23 PLOTONEB.M . . . . .	71
B.2.24 SFAVGXSUB.M . . . . .	71
B.2.25 SFPLOTSUB.M . . . . .	71
B.2.26 PLOTONE.M . . . . .	71
B.2.27 SFPLOT.M . . . . .	71
B.2.28 SFAVGX.M . . . . .	72
B.2.29 AVGNAN2.M . . . . .	72
B.2.30 AVGNAN.M . . . . .	72
B.2.31 AVGINF.M . . . . .	72
B.2.32 MINNAN/MAXNAN.M . . . . .	72
 Bibliography . . . . .	 73
 Vita . . . . .	 75

## LIST OF FIGURES

Figure		Page
1.	Theoretical Slope Structure Function . . . . .	16
2.	Hartmann Wave Front Sensor . . . . .	21
3.	Array of Point Spread Functions . . . . .	22
4.	Experimental Optical Setup . . . . .	26
5.	Phase Screen From an H-WFS . . . . .	27
6.	Laboratory Experiment Optical Bench Setup . . . . .	30
7.	Slope Averages . . . . .	31
8.	Slope Variances . . . . .	32
9.	Slope Structure Functions: Homogeneity . . . . .	34
10.	Slope Structure Functions: Isotropy . . . . .	35
11.	Slope Structure Function Comparison . . . . .	37
12.	Correlation Coefficient From Lab Data . . . . .	39
13.	Probability Density Distribution of Intensity . . . . .	40
14.	Slope Averages: Data Set 004 . . . . .	45
15.	Slope Variances: Data Set 004 . . . . .	46
16.	Slope Structure Function Comparison . . . . .	47
17.	Data Set 005: Slope Averages . . . . .	55
18.	Data Set 005: Slope Variances . . . . .	56
19.	Data Set 005: Slope Structure Function Comparison . . . . .	57
20.	Data Set 008: Slope Structure Function Comparison . . . . .	58

Figure		Page
21.	Data Set 009: Slope Structure Function Comparison . . . . .	59
22.	Data Set 024: Slope Structure Function Comparison . . . . .	60
23.	Data Set 507: Intensity Probability . . . . .	61
24.	Data Set 507: Slope Structure Function Comparison . . . . .	62
25.	Data Set 523: Slope Structure Function Comparison . . . . .	63
26.	Data Set 524: Slope Structure Function Comparison . . . . .	64

## LIST OF TABLES

Table		Page
1.	Summary of H-WFS image data sets presented. . . . .	44
2.	Summary of slope-method results from experimental image data sets. . . . .	48
3.	Summary of intensity-method results from experimental image data sets. . . . .	49

## LIST OF SYMBOLS

Symbol		Page
$\psi(\vec{x})$	Phase Fluctuation . . . . .	8
$\chi(\vec{x})$	Log-Amplitude Fluctuation . . . . .	8
$L_o$	Outer Scale . . . . .	9
$l_o$	Inner Scale . . . . .	9
$\Phi_n(\kappa)$	Power Spectral Density . . . . .	10
$C_n^2$	Atmospheric Structure Constant . . . . .	10
$E[\cdot]$	Expected Value Operator . . . . .	11
$k$	Wavenumber . . . . .	12
$r_o$	Fried Parameter, coherence diameter . . . . .	12
$I_o$	Mean Intensity . . . . .	17
$p_I(I)$	Probability Density of Intensity . . . . .	17
$\sigma_\chi^2$	Log Amplitude Variance . . . . .	17
$D_\chi(\Delta x)$	Log-Amplitude Structure Function . . . . .	18
$\theta$	Wave Front Tilt . . . . .	22
$f$	Focal Length . . . . .	22
$\lambda$	Wavelength . . . . .	23
$s$	Wave Front Slope . . . . .	23
$D_x(\vec{x}_n, \vec{x}_k)$	Slope Structure Function . . . . .	28
$\rho$	Correlation Coefficient . . . . .	38

# CHAPTER I

## INTRODUCTION

The effects of atmospheric turbulence on the propagation of light have long been recognized. This phenomenon imposes a limit on the resolution achievable in imaging through the earth's atmosphere, a limit nearly independent of the size of the telescope being used. Understanding atmospheric turbulence can provide ways to not only account for, but even correct for, optical system degradations caused by propagation through atmospheric turbulence. Both phase and intensity can be affected by this propagation.

### *1.1 Background*

Ground-based imaging of space objects was the first area in which problems were noticed that occurred as a result of atmospheric turbulence. During the time of Isaac Newton it was understood that the point spread function obtained in using a telescope to examine a star was broader than the point spread attainable under laboratory conditions. Newton correctly attributed these effects to "tremors" in the atmosphere [1]:

“If the theory of making Telescopes could at length be fully brought into Practice, yet would there be certain Bounds beyond which Telescopes could not perform. For the air through which we look upon the Stars, is in perpetual Tremor; as may be seen by the tremulous Motion of Shadows cast from high Towers, and by the twinkling of the fix’d stars.”

The source of this limitation is the random distribution of pockets of air in the atmosphere with different temperatures and thus differing refractive indices. The motion of these pockets of air is called turbulence. An optical field that encounters the atmosphere will have its phase altered by this distribution. Light from a distant object such as a star is well represented by a plane wave, and this plane of constant phase will become randomly perturbed after passing through the atmosphere. *Adaptive optics* can be used to compensate for this problem by using optical elements to correct for the phase aberrations [2]. After propagating some distance as a corrupted phase front, different portions of a wave will interfere with each other. The resulting pattern of light and dark regions is called scintillation. Because the nature of this disturbance is intensity differences and not phase aberrations, correction of the phase front by normal adaptive optics methods will not improve the signal.

Atmospheric turbulence has been described statistically by Kolmogorov. He developed a power spectral density (PSD) to describe the spatial frequency statistics of the index of refraction variations present in the atmosphere. Fried derived a structure function based on Kolmogorov’s PSD. A structure function is a second order statistic closely related to a correlation function, and Fried’s wave structure

function quantified the phase variations present on a wavefront passing through the atmosphere.

Studies are now under way to examine how atmospheric effects may impact applications other than imaging. High energy lasers may be utilized in a variety of ways under free-space conditions. These areas would involve propagation of laser beams over long paths in both vertical and horizontal directions. Scintillation of the laser beam will result in the reduction of power delivered to the desired location and thus limit effectiveness [3]. Knowledge of the consequences involved in passing through turbulence is therefore crucial in determining the applicability of this technology.

Free-space optical communications is another important area of study due to the low probability of intercept, long range, and high data rates available. Horizontal propagation at various altitudes in the atmosphere is a major factor in this work, and the possibility that communications could be affected requires greater understanding of the problems scintillation and phase degradation may cause [4].

## *1.2 Previous Work*

A large body of work exists in the field of optical atmospheric propagation. Much of this work deals with imaging vertically through turbulence, but horizontal paths are currently receiving more study. In 1985 experiments called HAVE LACE were performed by the Air Force's Wright Laboratory. Wright Lab studied scin-



tillation effects on air-to-air optical communications [4]. These studies dealt with high-altitude propagation between aircraft, but did not characterize the phase perturbations that give rise to this scintillation.

In 1993 the Air Force's Phillips Laboratory performed experiments called ABLEX to characterize turbulence in the upper atmosphere. ABLEX used a temperature probe mounted on an aircraft to monitor the random pockets of air and indirectly measure turbulence strength [3]. Later experiments named ABLE ACE were also conducted by Phillips Laboratory during January and March of 1995. A laser beam was propagated between two aircraft flying above and around the stratosphere. The result was a collection of data sets which contain camera images from a Shack-Hartmann Wave Front Sensor (H-WFS). A Shack-Hartmann WFS can be used to measure both wavefront phase and scintillation. The images taken exhibit both phase variations and scintillation due to turbulent air. Data analysis has been performed on these images [5]. Preliminary results indicate that the measured turbulence follows theoretical models.

### *1.3 The Maui Experiment*

In the summer of 1995, Wright Laboratory conducted a variety of experiments in Hawaii dealing with optical communications. Laser light at a wavelength of 810 nm was sent and received from both Mts. Haleakala on the island of Maui and Mauna Loa on the island of Hawaii. The path between these two sites ranged in

altitude from 9,000 to 11,000 ft and was 150 km in length, the majority of which was over water. This altitude is much lower than that at which the bulk of the previous work in this field has been conducted [3, 4, 5, 6]. Ground-based laser transmitters and receivers will encounter turbulence of this type, and its characterization is very important. Primarily, it must be determined if the theory developed for weak turbulence applies to these conditions. It is believed that scintillation under low altitude horizontal propagation is stronger than that encountered in more traditional vertical experiments and in higher altitude horizontal experiments. Both intensity variations and phase variations must be studied to gain a clear picture of the turbulence.

Experiments incorporating a H-WFS use an array of lenslets and a camera to capture light that has passed through turbulence. The wave front phase cannot be directly determined. Instead, measurements of the slope of the wave front are found for various locations in the pupil, and the phase front is inferred from these slopes. Phase reconstruction has been shown to work well in laboratory conditions [7], but is computationally intensive and has been found to be sensitive to errors in the slope measurements. This thesis will deal with the study of phase perturbations on the slope level. Because a H-WFS uses a CCD camera, scintillation measurements are easy to take simultaneously with phase information. This capability makes the Hartmann Sensor a versatile component in the adaptive optics field.

## 1.4 *Problem Description And Goals*

The goal of this thesis is to characterize atmospheric turbulence over a long horizontal path at a low altitude using a Hartmann Wave Front Sensor. Due to the random nature of turbulence, statistical analysis will play a large part in this characterization. This analysis will include the use of structure functions. The steps used in this analysis will be:

- Determine wave front slope values from the H-WFS images.
- Estimate slope structure functions from these slope values.
- Analyze the structure functions for their fit to theory.
- Characterize intensity variations due to signal scintillation.
- Determine various statistical quantities dealing with scintillation and compare with theory.

Results from this analysis indicate that the turbulence present under the conditions being studied is dominated by scintillation, and pure phase processing of the light received will be inadequate.

## 1.5 *Summary*

Chapter II provides the physical explanation and theoretical characterization of atmospheric turbulence. The H-WFS measurement process incorporating the statistical study of both phase and intensity fluctuations is presented in Chapter III.

Chapter IV introduces the data sets taken for the Hawaii experiment, and presents results for the characterization of low altitude long horizontal optical paths. Chapter V discusses conclusions and provides suggestions for further research.

## CHAPTER II

### THEORY

The two most important areas in the study of turbulence and its effects on light are wave front phase variations and intensity variations. The optical field  $u(\vec{x})$  representing light that has passed through the atmosphere must incorporate both phase and amplitude components. We will let  $\psi(\vec{x})$  account for the phase fluctuations of the field, and  $\chi(\vec{x})$  account for the logarithm of the field amplitude fluctuations. The field can then be written as [8]

$$u(\vec{x}) = A_o(\vec{x}) \exp[\chi(\vec{x}) + j\psi(\vec{x})], \quad (1)$$

where  $A_o(\vec{x})$  represents the nominal amplitude of the field. This chapter contains a description of atmospheric turbulence and the methods used to study the effects of turbulence on this optical field using a Hartmann Wave Front Sensor (H-WFS).

## 2.1 Atmospheric Turbulence

The Earth's atmosphere goes through differential heating and cooling, bringing about large scale variations in temperature and pressure. Resultant air movement distributes energy among these pockets and breaks them down into smaller sizes, causing random motion of complex pockets of air with varying refractive indices. This motion is called *turbulence*. Because the index of refraction of air is sensitive to temperature, these pockets have random effects on the speed of light propagating through them and thus change the phase of the light. This is explained very well by Roggemann et al [9]. The size of these pockets becomes smaller until viscous effects dominate, motion becomes smooth and regular, and the flow is termed laminar [2].

The theoretical foundations in atmospheric turbulence were performed by Kolmogorov, Tatarski, and Fried. Kolmogorov [10] developed a power spectral density (PSD) describing the spatial frequency statistics of the atmosphere's index of refraction variations. This theory holds for a specific range of spatial frequencies  $\kappa$  called the *inertial subrange*. These spatial frequencies correspond to the size of the turbulent eddies  $L$  as  $L = 2\pi/\kappa$ . The inertial subrange extends from the largest eddy size  $L_o = 2\pi/\kappa_o$  called the outer scale, to the smallest size  $l_o = 2\pi/\kappa_m$  called the inner scale. Typical values for  $L_o$  range from 1 to 100 m, and values for  $l_o$  are on the order of a few millimeters [11]. The Kolmogorov PSD is given by

$$\Phi_n(\kappa) = 0.033 C_n^2 \kappa^{-11/3}, \quad (2)$$

where  $\Phi_n(\kappa)$  is the PSD and  $C_n^2$  is called the *structure constant* of the fluctuations in the air's refractive index [11].  $C_n^2$  characterizes the strength of these fluctuations, and has been determined experimentally. Many different models exist for this constant, based mainly on altitude above the surface of the earth [2, 12]. Typical values for  $C_n^2$  are on the order of  $10^{-16} \text{ m}^{-2/3}$ . Problems present in Kolmogorov's PSD have been corrected in other models, most notably the von Karman spectrum. Tatarski later applied Kolmogorov's results to wave propagation and imaging through distributions of random indices of refraction [13]. Fried then extended these theories to the optics engineering community and specific atmospheric optics problems [8].

The Kolmogorov PSD forms a Fourier transform pair with the autocorrelation of the refractive index. Thus the statistics describing turbulence may be done in spectral or spatial representations. These statistics describe a three dimensional random process. Two important definitions related to this process are homogeneity and isotropy. A random process is said to be homogeneous if it is spatially stationary; i.e., it does not depend on location. Isotropy holds if the process is also spherically symmetric. The index of refraction fluctuations in the atmosphere are generally assumed to be homogeneous and isotropic, and thus don't depend on either location or direction. Many experiments have been done that support this assumption [5, 14], but it does not always hold.

## 2.2 Structure Functions

One quantity widely used to study the spatial characteristics of a random process is the structure function. This quantity appears often in the field of turbulence, and understanding it is very important. A structure function can be thought of as an expected value for the strength of variations present in a random process, or alternately as the mean square difference between two realizations. Tatarski defined an expression for the structure function of the index of refraction for atmospheric turbulence [13]. This structure function is expressed as

$$D_n(\vec{r}_1, \vec{r}_2) = E \left[ (n_1(\vec{r}_1) - n_2(\vec{r}_2))^2 \right], \quad (3)$$

with  $D_n(\vec{r}_1, \vec{r}_2)$  as the structure function of the index of refraction  $n$  at locations identified by the vectors  $\vec{r}_1$  and  $\vec{r}_2$ , and  $E[\cdot]$  representing the expected value operator. If the refractive index variations are homogeneous as described above, the structure function becomes a function only of the vector difference between  $\vec{r}_1$  and  $\vec{r}_2$ . If the variations are also isotropic, the structure function will depend only on the magnitude  $r$  of the separation between points  $\vec{r}_1$  and  $\vec{r}_2$ , and we write  $D(r)$ , as the structure function is a function only of the separation  $r = |\vec{r}_1 - \vec{r}_2|$ .

*2.2.1 Phase Structure Functions.* Tatarski also extended the theory of index of refraction structure functions to a plane wave propagating through the atmosphere. The wavefront phase distortion caused by this propagation can be charac-



terized by the phase structure function,  $D_\psi(\Delta\vec{x}) = E [(\psi(\vec{x}) - \psi(\vec{x} + \Delta\vec{x}))^2]$ , where  $\Delta\vec{x}$  is the spatial separation between the points of interest. Using Kolmogorov's PSD, Fried derived a phase structure function for a plane wave propagating through turbulence as [8]

$$D_\psi(\Delta\vec{x}) = 2.91 k^2 z C_n^2 |\Delta\vec{x}|^{5/3}. \quad (4)$$

Here  $k$  is the wavenumber  $\frac{2\pi}{\lambda}$  and  $z$  is the length of the path through the turbulence. Note that any one of four things will cause an increase in the structure function and thus reflect an increase in the strength of the turbulence effects: a shorter wavelength, a longer optical path, stronger refractive index fluctuations, or a greater separation between the points in the pupil being studied (resulting in the points being less correlated).

Fried went on to express this phase structure function in terms of the *Fried parameter*  $r_o$ , also commonly referred to as the atmospheric coherence diameter [8]. This value can be interpreted as the aperture size beyond which an increase in size will not improve resolution. Increasing the aperture size beyond  $r_o$  in diameter will improve light gathering capabilities but not resolution. Typical values for the Fried parameter are around 1 – 5 cm for poor seeing conditions, and near 20 – 30 cm for good seeing conditions [11]. The Fried parameter is given by [2]

$$r_o = 0.185 \left( \frac{4\pi^2}{k^2 C_n^2 z} \right)^{3/5}. \quad (5)$$

Using this definition to rewrite Eq. (4) yields the most common expression for the phase structure function [2]:

$$D_\psi(\Delta x) = 6.88 \left( \left| \frac{\Delta \vec{x}}{r_o} \right| \right)^{5/3}. \quad (6)$$

*2.2.2 Slope Structure Functions.* Various methods exist for sensing and measuring wavefront perturbations caused by the atmosphere, from differential imaging [15] to interferometry [16]. Recently, a Hartmann Wave Front Sensor (H-WFS) has been used for this purpose [17]. The Hartmann Sensor will be discussed in more detail in Section 3.1, but a brief introduction is necessary here to develop supporting theoretical work. A H-WFS measures the gradient of the wavefront phase across small regions of the wave front. These small regions are called subapertures. The gradient in both the  $x$  and  $y$  directions are found and called slopes, and the entire phase front is then reconstructed from these individual slope measurements. Recently work has been done to bypass the phase reconstruction step and perform statistical analysis on the slope values themselves [5]. Phase structure functions can be replaced by slope structure functions, keeping in mind that the slope structure function is theoretically related to the phase structure function [5].

Let the WFS slope measurement from the  $n^{th}$  subaperture located by  $\vec{x}_n$  be expressed as  $s^{\hat{x}}$  or  $s^{\hat{y}}$ , where  $\hat{x}$  or  $\hat{y}$  represents the direction of the tilt being measured. For discussion purposes consider the definition of the subaperture slope measurement

$s^{\hat{x}}$  given by [18]

$$s^{\hat{x}}(\vec{x}_n, t) = \int_{pupil} W(\vec{x}' - \vec{x}_n) (\nabla \psi(\vec{x}', t) \cdot \hat{x}) d\vec{x}', \quad (7)$$

where  $\nabla$  is the gradient operator,  $\psi(\vec{x}', t)$  is the wave front phase aberration imposed by the atmosphere as a function of time, and  $W$  is the pupil function operator. This equation exhibits how the geometric representation of the pupil function impacts the light passing through it, and how the gradient of the phase front is quantified. Wallner [18] shows through integration by parts that Eq. (7) can be written as

$$s^{\hat{x}}(\vec{x}_n, t) = - \int_{pupil} (\nabla W(\vec{x}' - \vec{x}_n) \cdot \hat{x}) \psi(\vec{x}', t) d\vec{x}'. \quad (8)$$

The slope structure function  $D_x$  is then defined as

$$D_x(\vec{x}_n, \vec{x}_k, t) = E \left[ \left( s^{\hat{x}}(\vec{x}_n, t) - s^{\hat{x}}(\vec{x}_k, t) \right)^2 \right]. \quad (9)$$

where  $E[\cdot]$  represents the expectation operator. By expanding Eqs. (8) and (9), and using Eq. (6) in an intermediate step, Silbaugh was able to derive an expression for the slope structure function using a Hartmann WFS with square subapertures of size  $d$  [19]:

$$\begin{aligned}
D_x(\Delta x, \Delta y) &= 6.88 d^{-2} \left( \frac{d}{r_o} \right)^{5/3} \int du' \text{tri}[u'] \\
&\quad \left\{ \left[ 2 |\Delta x, u' + \Delta y|^{5/3} - |\Delta x - 1, u' + \Delta y|^{5/3} - |\Delta x + 1, u' + \Delta y|^{5/3} \right] \right. \\
&\quad \left. - 2 \left[ |0, u'|^{5/3} - |1, u'|^{5/3} \right] \right\}
\end{aligned} \tag{10}$$

where  $\text{tri}[u]$  is a triangle function defined as

$$\text{tri}[u] = \begin{cases} 1 - |u| & |u| \leq 1 \\ 0 & \text{else} \end{cases}, \tag{11}$$

and  $|x, y| = \sqrt{x^2 + y^2}$ . The terms  $\Delta x$  and  $\Delta y$  represent the spatial separation of the subaperture slope measurements normalized by  $d$ . The dependence on the coherence diameter  $r_o$  and the subaperture dimension  $d$  are easily studied here as they are outside the integral. Figure 1 shows theoretical slope structure functions found for slopes in the  $\hat{x}$  direction using subaperture separations  $(\Delta x, \Delta y)$  only in the  $x$ ,  $y$ , and  $45^\circ$  directions. These curves were found using an  $r_o$  value of 5.0 cm. Similar curves exist for slopes in the  $y$  direction with the  $x$  and  $y$  curves interchanged. For no shift (comparing a slope value with itself) the structure function necessarily vanishes. For increasingly large separations the function asymptotically approaches a fixed value until the separation is so large that the corresponding slopes are no

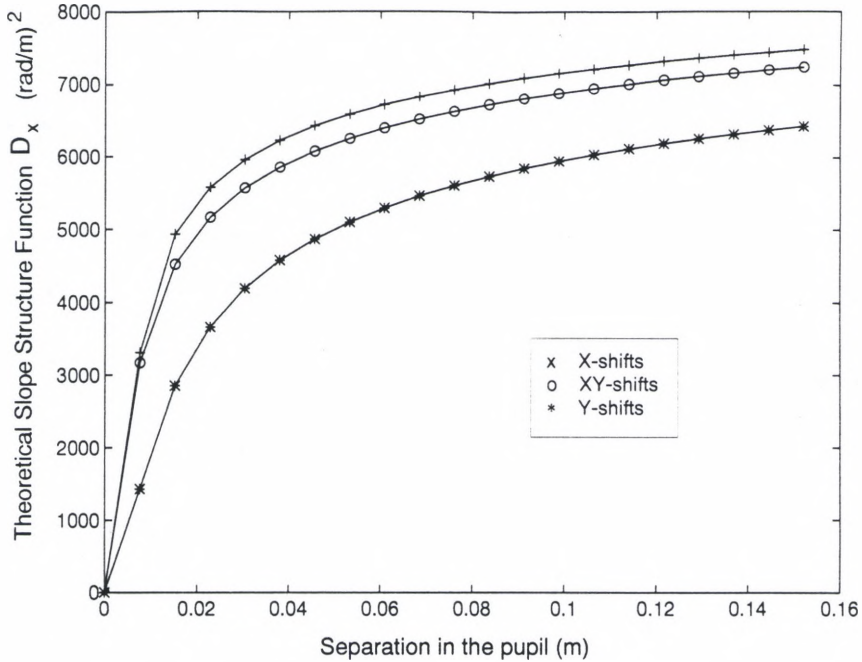


Figure 1. Theoretical slope structure function for  $x$ ,  $y$ , and 45 deg shifts as a function of subaperture separation.

longer correlated. This asymptote occurs at a value of the structure function equal to twice the mean square value of the slopes.

### 2.3 Scintillation

Phase fluctuations imposed by the atmosphere are only one part of the study of turbulence. If the turbulence present is strong enough, or if the propagation length through the turbulence is long enough, slight refraction that results from the phase changes on the wavefront causes the optical fields to interfere. Both phase and amplitude perturbations result. A camera that is imaging the telescope pupil detects intensity changes, and these intensity fluctuations are referred to as scintillation. Re-examining Eq. (1) and dropping the spatial dependence, as we may do if the

turbulence is homogeneous, we find the intensity of the optical field can be expressed as

$$I = A_o^2 \exp(2\chi). \quad (12)$$

We write the amplitude  $A_o^2$  as  $I_o$ . Then solving for the log amplitude perturbation  $\chi$  we get

$$\chi = \frac{1}{2} \ln \left( \frac{I}{I_o} \right). \quad (13)$$

When we make the assumption that  $\chi$  has a Gaussian distribution and  $I$  has a mean value (or expectation value) of  $I_o$  [11], we find

$$E[I] = I_o E \left[ e^{2\chi} \right] = I_o. \quad (14)$$

The Gaussian nature of  $\chi$  results in an intensity probability density function  $p_I(I)$ , given as

$$p_I(I) = \frac{1}{2\sqrt{2\pi}\sigma_\chi I} \exp \left\{ -\frac{\left( \frac{1}{2} \ln \frac{I}{I_o} - \bar{\chi} \right)^2}{2\sigma_\chi^2} \right\}, \quad (15)$$

where  $\bar{\chi}$  is the mean value of the log-amplitude distribution and  $\sigma_\chi^2$  is the variance [11]. This probability density function can be used to compare measured intensity fluctuations to theory.

Finally, we note that for any real-valued Gaussian random variable  $z$  and any complex constant  $\mathbf{a}$ , the expectation value of an exponential expression is given in [2]

by

$$E[e^{\mathbf{a}z}] = \exp\left\{\mathbf{a}\bar{z} + \frac{1}{2}\mathbf{a}^2\sigma_z^2\right\}. \quad (16)$$

Applying Eq. (16) to Eq. (14) we find

$$\bar{I} = I_o e^{2\bar{\chi} + 2\sigma_\chi^2} = I_o, \quad (17)$$

or equivalently

$$\bar{\chi} = -\sigma_\chi^2. \quad (18)$$

We will examine our results to see if they follow this equality.

Along with the phase-induced structure function, a second important structure function is for the log-amplitude intensity fluctuations. This function is denoted by  $D_\chi(\Delta x)$ , and defined by [2]

$$D_\chi(\Delta x) = E\left[(\chi(x) - \chi(x + \Delta x))^2\right]. \quad (19)$$

The sum of the amplitude and phase structure functions is called the wave structure function,  $D(\Delta x) = D_\chi(\Delta x) + D_\psi(\Delta x)$ . In practice, the phase and intensity structure functions will have varying importance in describing the optical signal. For short optical paths phase aspects will dominate, while longer paths will be more influenced by intensity.

The basis for much of the above work rests on the Rytov approximation, and the generality of the approximation and its results are of great importance. This approximation holds in the case of weak fluctuations of the amplitude, and implies that  $\chi$  obeys log-normal statistics. The assumption of weak fluctuation is generally agreed to hold when the log-intensity variance is smaller than about 0.3. For Kolmogorov turbulence, this criterion becomes [11]

$$\sigma_{\ln \frac{I}{I_0}}^2 = 1.23 C_n^2 k^{7/6} z^{11/6} < 0.3. \quad (20)$$

Now using Eq. (13) and the definition of the variance we see that

$$\sigma_{\ln \frac{I}{I_0}}^2 = E \left[ \ln \left( \frac{I}{I_0} \right)^2 - \overline{\ln \left( \frac{I}{I_0} \right)^2} \right] = E [4\chi^2 - 4\bar{\chi}^2] = 4\sigma_\chi^2. \quad (21)$$

Thus the criterion for weak turbulence becomes

$$\sigma_\chi^2 < 0.075. \quad (22)$$

Examining the variance of  $\chi$  is an important tool for characterizing atmospheric turbulence.



## *CHAPTER III*

### STATISTICAL METHODS

In Chapter II we discussed the two main topics used to describe atmospheric turbulence. Now we study the data taken in both the laboratory and in Hawaii using a variety of statistical analysis methods. Using more than one method allows for the comparison of results achieved through different means. Both intensity fluctuations and phase perturbations were noticed in the data. Existing theory and the ability of a Hartmann Wave Front Sensor (H-WFS) to measure each of these phenomena allowed for research in both areas. This flexibility is a strong endorsement of the Hartmann technology. When data from one method is unreliable, as we will see in this thesis, the other method will be available.

In the next section we describe a Hartmann Sensor and the computer methods used to utilize this sensor. The following two sections explain the statistical methods developed to analyze Hartmann data, both for phase and intensity fluctuations.

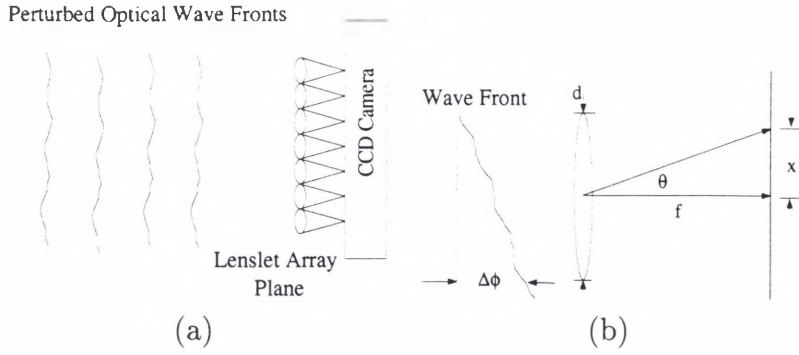


Figure 2. Schematic of a Hartmann Wave Front Sensor: (a) Full view of an H-WFS with a perturbed wavefront encountering the lenslet array; and (b) View of a single subaperture with wave front tilt  $\theta$ , phase delay across the subaperture of  $\Delta\Phi$  and centroided spot displacement  $x$ .

### 3.1 Hartmann Wave Front Sensors

One method for determining the phase of a wave front is through the use of a Hartmann Wave Front Sensor. This method uses Wave Front Sensor camera images (WFS images) to reconstruct a phase map of the wave front. A H-WFS does not measure the phase directly, but instead spatially divides the aperture into an array of subapertures and finds the average wave front phase gradient in each subaperture. These gradients are referred to as slopes [5].

A Hartmann sensor is shown in Fig. 2 (a) and consists of a CCD camera and a two-dimensional lenslet array, where each element of the lenslet array constitutes a subaperture. The array of lenses focuses incident light into an array of images on the camera and a pattern of point-spread functions results. An example of such an image is shown in Fig. 3. The sensor in the experiments discussed here used a lenslet grid of  $20 \times 20$  square subapertures measuring  $203 \mu\text{m}$  on a side and a CCD camera having a  $256 \times 256$  array of pixels, each  $16 \mu\text{m}$  on a side. The focal length

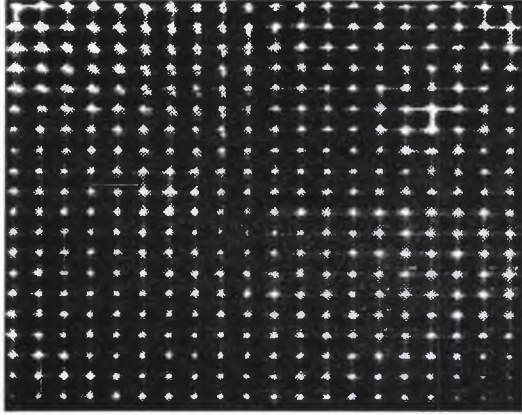


Figure 3. Array of Point Spread Functions imaged by a Hartmann Wave Front Sensor. The location and intensity of each spot provides information about the wavefront.

of each of these lenslets was 7.8 mm. For the given geometry, a focused spot will cover somewhere between 10 to 20 pixels.

The location of a focused spot in a subaperture is proportional to the average tilt  $\theta$  of the portion of the wave front incident on that subaperture. The spot location in each dimension is found by centroiding the pixel intensities in the subaperture [2]. The wave front tilt  $\theta$  in the subaperture is written as

$$\theta = \tan^{-1} \left( \frac{x}{f} \right), \quad (23)$$

where  $f$  is the focal length of an individual lenslet and  $x$  is the spot displacement from the center of the subaperture (see Fig. 2 (b)) found by centroiding. Often the  $\tan^{-1}(\frac{x}{f})$  is approximated as simply  $\frac{x}{f}$  due to the small angles involved. The delay

present in the phase front from one side of the subaperture to the other is given by

$\Delta\Phi$ :

$$\Delta\Phi = \frac{2\pi\theta d}{\lambda} \quad (24)$$

where  $d$  is the size of a subaperture and  $\lambda$  is the wavelength of the light. The wave front slope,  $s$  (in  $rad/m$ ), is the normalized phase delay and is calculated using

$$s = \frac{2\pi\theta}{\lambda}, \quad (25)$$

For this experiment the wavelength was 810 nm. Varying atmospheric perturbations on different portions of the wave front cause these slope values to change in time. The slopes are assumed to be zero mean [12].

*3.1.1 Camera Image Processing.* The first step in processing images from a CCD camera is removal of the camera's effects on the image. Thermal noise in a CCD results in extraneous charge carriers, called dark current. Spatial variations in the response to light from one pixel to another, called flat-field response, also affects processing. These problems are accounted for by exposing the camera separately to a dark field and a uniform flat-field. A corrected image is then found by forming the difference between the object and dark field images and dividing the result, pixel by pixel, by the flat field [20].

Various methods were used to determine the validity of camera images and improve the reliability and accuracy of the processing in this work. First, a threshold

was established for the intensity in a pixel. If a pixel had too little light the pixel was made completely dark to improve the contrast of a valid spot. The image as a whole was also required to have a certain minimum amount of light. This was important because scintillation caused some images to be almost completely dark, with too little light to adequately define a complete array of point spread functions. A validity check was also performed on the shape of the peak of each focused spot. This check worked as a type of a signal-to-noise ratio. The value of the ratio was defined by

$$SNR = \frac{\bar{\eta}}{l \sqrt{2\bar{\eta} \sum_i \sum_j i^2 \frac{\lambda_{ij}}{\bar{\eta}} + 2N^2 \sigma_e^2}} \quad (26)$$

where  $\bar{\eta}$  is the average total photon count per subaperture,  $N^2$  is the total number of pixels per subaperture,  $\sigma_e^2$  is the variance of the camera's pixel read noise,  $l$  is the pixel separation, and  $\lambda_{ij}$  represents the photon count for the pixel indexed in the subaperture by  $i$  and  $j$ . The value resulting from this equation was examined so that an identifiable peak must be present to be labeled a valid focused spot. An  $SNR$  value that was too low implied that the light in the subaperture was too dim and randomly distributed. In this case the subaperture was made invalid.

Finally, besides the centroiding method mentioned above, each spot was located by a second method. By finding the pixel(s) with maximum intensity in a subaperture, and comparing the intensity of neighboring pixels, the location of a peak could be interpolated to sub-pixel accuracy. If the two methods of peak location did not match to within one pixel the subaperture was invalidated.

*3.1.2 Computer Methods and Phase Reconstruction.* Once the slope values are obtained, they can be multiplied by a reconstruction matrix to arrive at an array of phase values [9, 21]. The size of this array of phase values depends on the number of points in the pupil, called basis functions, at which the phase is desired. For this experiment, an array of  $11 \times 11$  basis functions was assumed. This phase map was then expanded into a  $41 \times 41$  array using weighting functions to interpolate between neighboring phase values. This final phase map contains spatial information on the phase of the incident wave front.

After calibration, the first step in computer processing is initial determination of the subaperture locations in pixel space on the image. Because a H-WFS can only determine relative phase difference and not absolute phase, we initially arbitrarily locate these subapertures. Centroiding is then done for each subaperture of each image, once in the x-direction and once in the y-direction. Averages are found for each subaperture, and these average x and y locations are used to move the subaperture locations such that each spot is in the center of its subaperture on average. Performing this re-centering serves to remove overall tilt from the phase screen. This overall tilt cannot be trusted as having come from atmospheric effects because other factors such as misalignment of the system with the source can result in similar but extraneous tilt. Once the subapertures are located correctly over the spots, the images are ready to be individually re-centroided using the new subaperture locations. This step results in slope values with zero-mean.

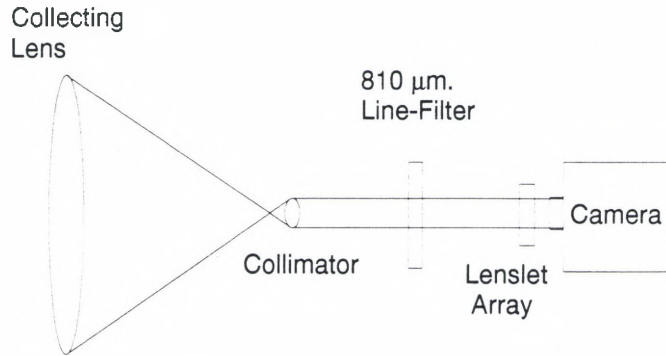


Figure 4. Optical setup used to acquire communications experiment images containing turbulence effects. The lens pair in front of the Hartmann Sensor relays light from the front pupil through the filter and to the camera.

In order to obtain as large a region of wave front data as possible, optics are used to magnify a region of interest in front of the system down to a size accessible to the camera. In this case a circle 2 cm in radius was taken down to 4 mm, as shown in Fig. 4. A problem that must be taken into account is misalignment of these elements with each other. To remove the effects of these optics on the signal, a reference image can be taken through the system with no turbulence present. The resultant slopes are removed from the actual experimental slopes, leaving only turbulence effects. If no reference imaging is possible, an average slope can be found in each direction for each subaperture. Because these slopes should be zero mean, this average contains the aberration effects of the optics. When this average is subtracted from the individual slopes the result is a signal containing only random turbulence effects. The final slope values are multiplied by a reconstruction matrix, and interpolation yields a phase screen as shown in Fig. 5. One screen exists for each image.

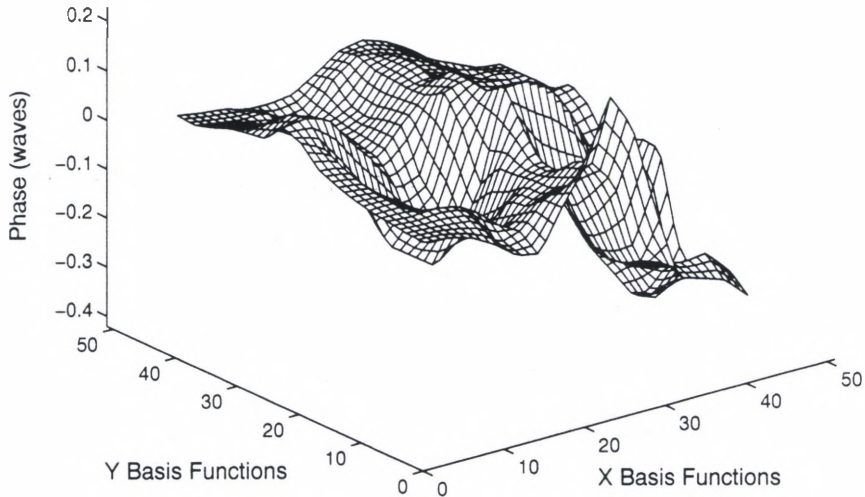


Figure 5. Reconstructed wave front phase screen from a Hartmann WFS for laboratory data.

### 3.2 Slope Statistics Analysis

Large ensembles of H-WFS images were taken to allow statistical analysis of atmospheric turbulence effects. Section 3.1.1 discussed some of the problems these images may have. Information from invalid subapertures were not used in any statistical methods. Unfortunately, leaving elements out of the ensemble decreases the confidence that may be placed in the statistical results. To quantify this, the Tchebycheff inequality was used, which computes a 95% *confidence interval* [22]

$$CI_{95} = \pm 4.47 \sqrt{\frac{\sigma^2}{n}}, \quad (27)$$

where  $\sigma^2$  is the variance of the value under study and  $n$  is the number of elements used from the ensemble. This interval will provide error bars for the data.



*3.2.1 Slope Structure Functions.* One of the most widely used and informative statistical analysis values for atmospheric turbulence is that of the structure function. A structure function reflects a measurement of spatial variation by finding the mean square difference between measurements at two locations, and is often performed on phase values. This topic was extended to slope value structure functions [5] to avoid the intensive phase reconstruction step. The slope structure function is computationally estimated by computing the mean square difference of the H-WFS slope measurements (from Eq. (25)) between any two subapertures in the pupil, and is written as

$$D_x(\vec{x}_n, \vec{x}_k) = \frac{1}{M} \sum_{m=1}^M [s^{\hat{x}}(\vec{x}_n, t_m) - s^{\hat{x}}(\vec{x}_k, t_m)]^2, \quad (28)$$

where  $D_x(\vec{x}_n, \vec{x}_k)$  is the estimated slope structure function,  $M$  is the number of independent realizations (measurements), and  $s^{\hat{x}}(\vec{x}_n, t_m)$  and  $s^{\hat{x}}(\vec{x}_k, t_m)$  are the slope measurements at the  $n$ th and  $k$ th subapertures centered at  $\vec{x}_n$  and  $\vec{x}_k$  and taken at time  $t_m$ .

For subapertures widely separated in the pupil, the number of realizations available for use in determining a structure function value is necessarily small due to the finite size of the pupil. This limitation causes confidence in the value of the structure function to decrease as separation increases. When comparison to theory is being done more confidence should be placed on the portions of the structure function dealing with smaller separation.

3.2.2 *Homogeneity-Isotropy.* As discussed earlier, perturbations of the slope due purely to atmospheric turbulence should have zero mean, and so we expect the slope averages to be zero across the aperture. Any non-zero average will correspond to a deterministic aberration and not to the atmosphere. Removal of the average slope should remove this deterministic aberration. The variance of these slopes is a second order statistical quantity. It will not cancel out, and will primarily be a function of turbulence strength. Examining the spatial characteristics of this variance reveals information about the validity of the assumptions made earlier dealing with homogeneity and isotropy. If the turbulence encountered is homogeneous, a representation of the slope variance should be uniform, that is smooth and flat, and large with respect to the average slope values. Similarly, slope structure functions for the same separation at different locations in the pupil should be nearly equal [5]. The estimator given in Eq. (28) makes no *a priori* assumptions about the homogeneity or isotropy of the data. In the event that the turbulence statistics are homogeneous, the estimate for the slope structure function for a given subaperture separation  $\Delta\vec{x}$  is given by additionally summing Eq (28) over all possible combinations of subapertures such that  $\Delta\vec{x} = \vec{x}_n - \vec{x}_k$ :

$$D_x(\Delta\vec{x}) = \frac{1}{MN} \sum_n^N \sum_{m=1}^M [s^{\hat{x}}(\vec{x}_n, t_m) - s^{\hat{x}}(\vec{x}_n - \Delta\vec{x}, t_m)]^2, \quad (29)$$

where  $N$  is the number of possible subaperture pairs that are separated by  $\Delta\vec{x}$ .

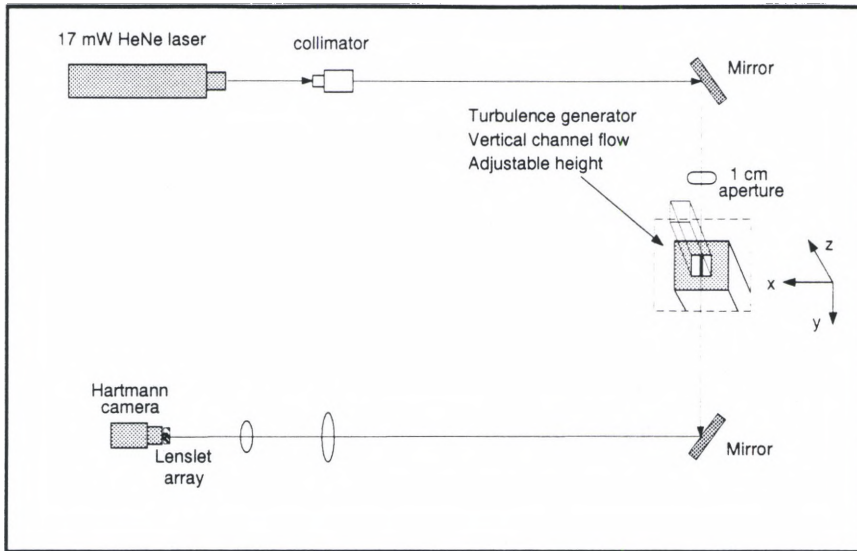
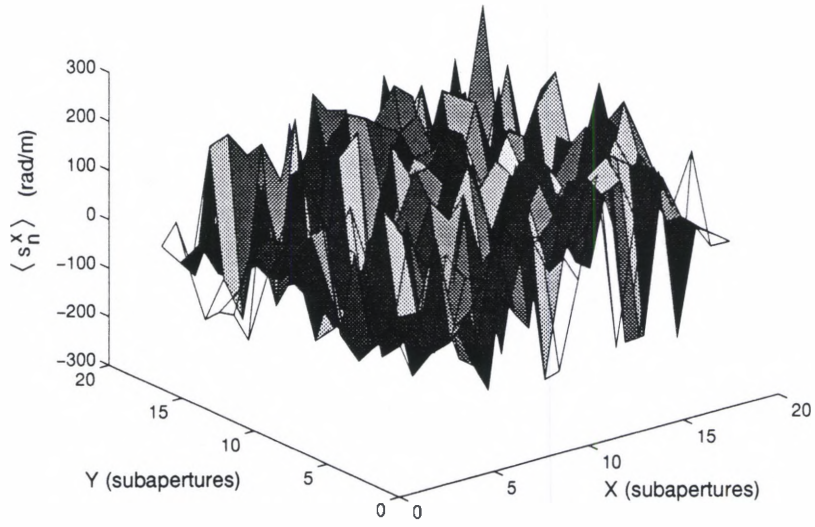
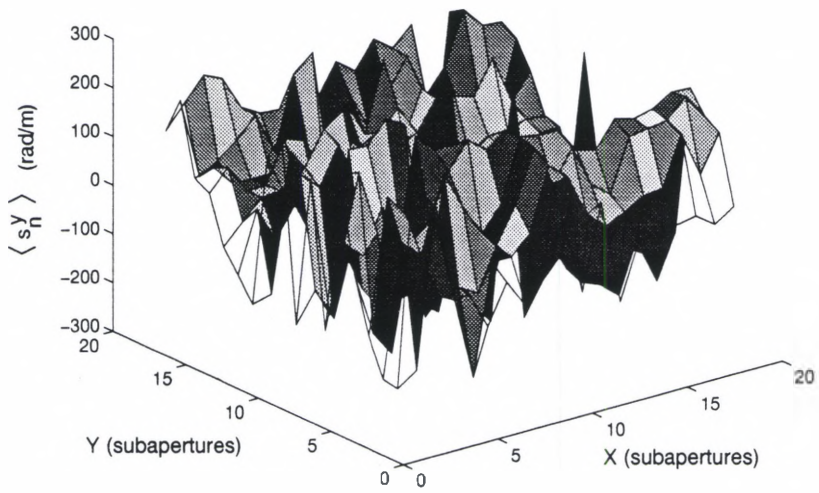


Figure 6. Optical Bench setup for laboratory experiments conducted on the H-WFS using a turbulent-mixing-layer turbulence generator.

Tests have been conducted under laboratory conditions to examine the operation of the Hartmann Sensor. In the lab, two different types of gases were brought together to create a turbulent mixing layer [23]. The gases chosen were helium and nitrogen, selected for the density ratio between them that provides large density fluctuations across the turbulent mixing layer. A collimated optical beam was passed through this mixing layer, picking up phase aberrations due to the mixing gases, and the resultant wavefront perturbations were sensed by a H-WFS. Figure 6 shows the optical bench setup containing the turbulence generator and the H-WFS. A doctoral dissertation performed by Patrick Gardner at Wright Patterson AFB discusses this turbulence and the wavefront sensing methods used in more detail. Figures 7 and 8 show slope averages  $\langle s_n^x \rangle$  and variances  $\langle (s_n^x)^2 \rangle$  for data taken under laboratory conditions. As expected, the average slopes are an order of magnitude smaller than

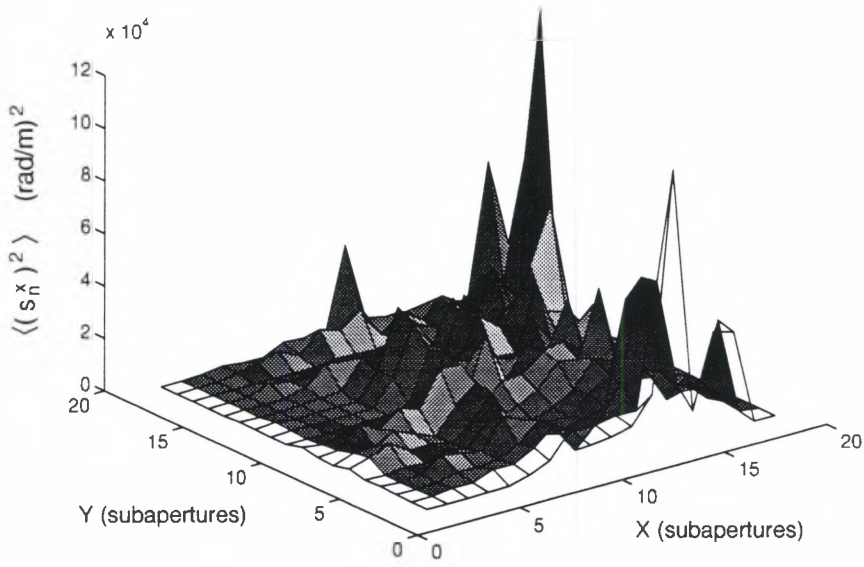


(a)

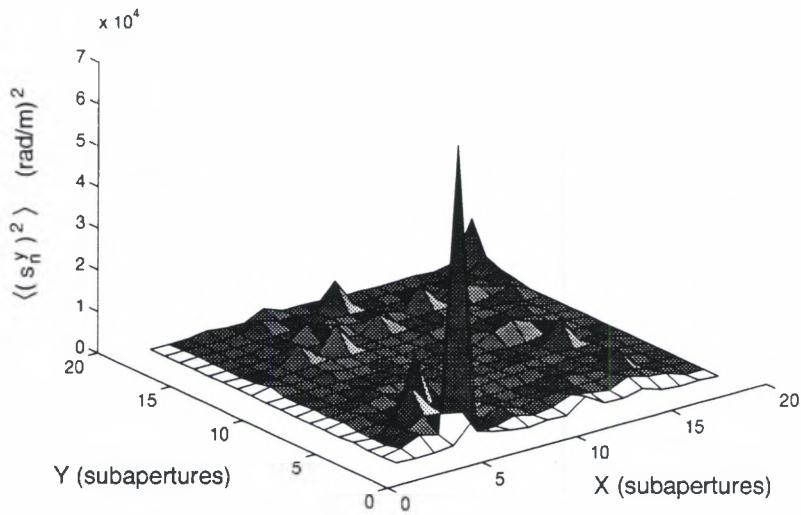


(b)

Figure 7. Average slope values from laboratory data (a) X-slope average,  $\langle s_n^x \rangle$  and (b) Y-slope average,  $\langle s_n^y \rangle$  across the subaperture.



(a)



(b)

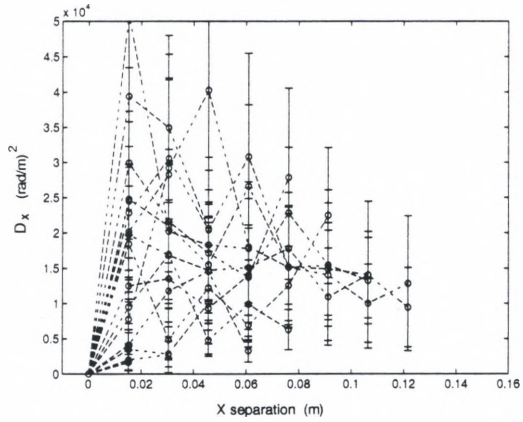
Figure 8. Slope variance values from laboratory data (a) X-slope variance,  $\langle (s_n^x)^2 \rangle$  and (b) Y-slope variance,  $\langle (s_n^y)^2 \rangle$  across the subaperture.

the variance, implying homogeneity. The variances are not very uniform across the pupil, however, leading us to believe that the data may not be homogeneous, and certainly doesn't appear to be isotropic. It will be seen that this pattern held for much of the data taken in the field.

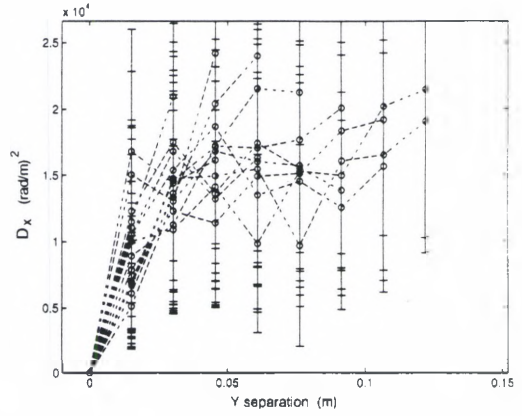
Figure 9 contains slope structure functions from the lab data. Each line represents a structure function for a different location in the pupil. These structure functions are for slopes in the  $x$  and  $y$  directions and separations in  $x$  and  $y$ . Homogeneous data should result in these lines clustering together. This behavior is seen in the lab data. Thus it cannot be positively determined with this data whether or not the laboratory data was homogeneous.

If the turbulence has been determined homogeneous, slope structure functions from various regions of the pupil may be averaged together. This averaging results in one structure function for each slope and separation direction, and tighter confidence intervals due to the increase in the number of samples being used. Comparison between these curves helps determine if the the turbulence is isotropic or not. Isotropic data will have structure functions that are similar in size and shape. Figure 10 shows self-slope structure functions that have been averaged across the aperture assuming the presence of homogeneity. The data does not exhibit isotropy, as the four functions do not match each other.

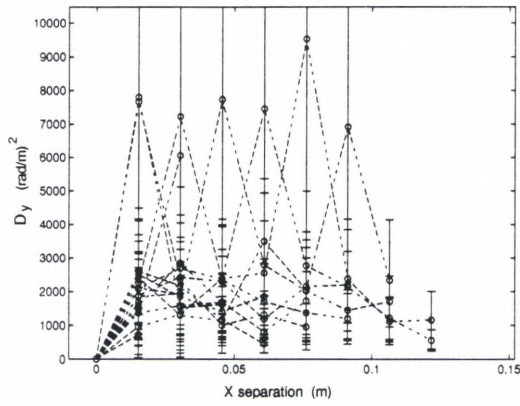
*3.2.3 Fried Parameter.* The desired result from these slope structure functions is the determination of the Fried Parameter  $r_o$ . One method is comparison of



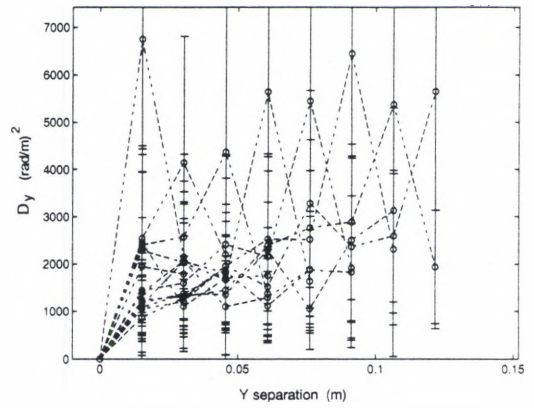
(a)



(b)



(c)



(d)

Figure 9. Experimental self-slope structure function homogeneity for laboratory data for: (a) X-slopes, x-shifts, (b) X-slopes, y-shifts, (c) Y-slopes, x-shifts, and (d) Y-slopes, y-shifts.

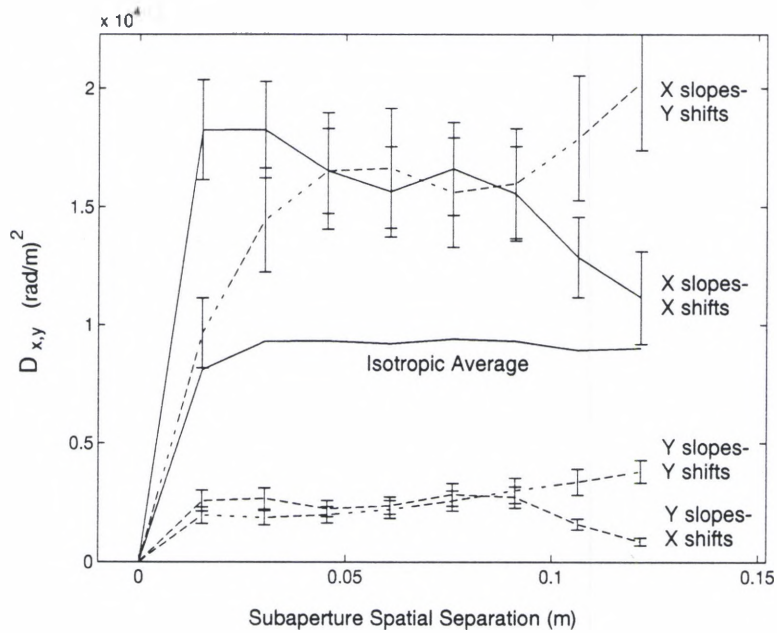


Figure 10. Experimental slope structure functions checking isotropy for laboratory data. Data for x and y slopes and shifts in the x and y directions is shown, as well as the average. Isotropy is not present.



theoretical and experimental structure functions. Equation (28) is used to find experimental structure functions, and Eq. (10) to find theoretical structure functions. Because the dependence on  $r_o$  in Eq. (10) is outside the integral the theoretical structure function is easily controlled. A coherence diameter for the experiment is found by varying  $r_o$  in the theoretical structure function and finding the value that minimizes the root-mean-square difference between theory and experiment. Figure 11 shows structure functions found both experimentally and theoretically for both  $x$  and  $y$  slopes with shifts in each direction. This data, while possibly homogeneous, does not appear to be isotropic. Values for the coherence diameter range from 0.025 m to 0.1 m for this laboratory-generated turbulence.

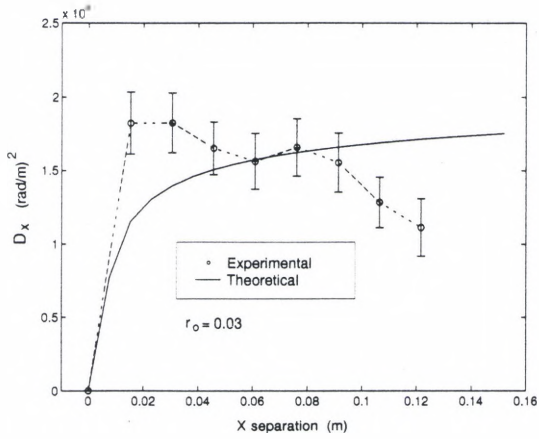
Another statistical method for estimating the Fried parameter is based on the mean square value of the slope  $\langle s^2 \rangle$  from a H-WFS with subapertures of size  $d$ . This mean square value is [17],

$$\langle s^2 \rangle = \frac{13.6183}{d^2} \left( \frac{d}{r_o} \right)^{5/3} \quad (30)$$

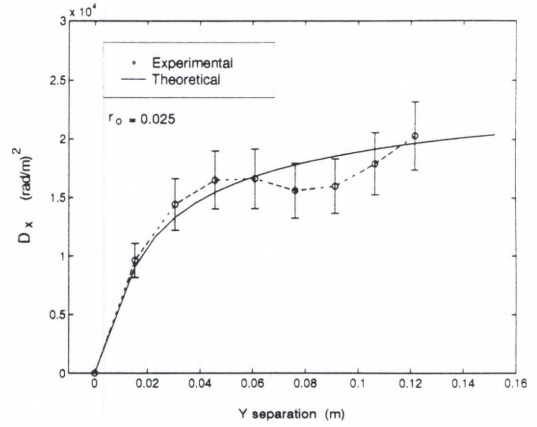
and solving for  $r_o$  gives

$$r_o = \left[ \frac{13.6183 d^{5/3}}{d^2 \langle s^2 \rangle} \right]^{3/5} \quad (31)$$

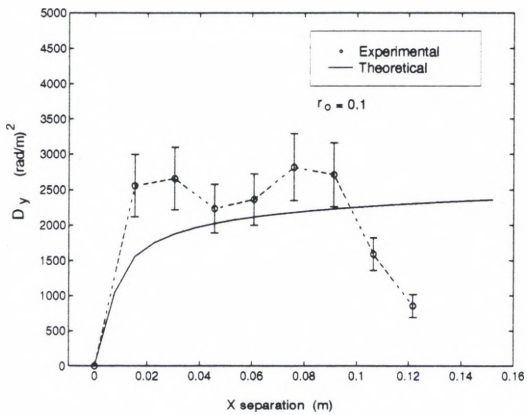
Equation (31) provides another way to arrive at values for the coherence diameter.



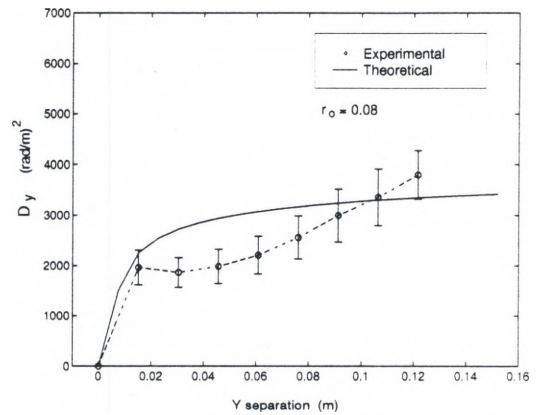
(a)



(b)



(c)



(d)

Figure 11. Self-slope structure functions for laboratory data fitted to theory: (a) X-slopes, x-shifts, (b) X-slopes, y-shifts, (c) Y-slopes, x-shifts, and (d) Y-slopes, y-shifts.

### 3.3 Scintillation Statistics

The scintillation present in some WFS images causes the determination of slope values to be suspect. In these cases the study of the intensity variations themselves may be used to gain insight into the turbulence present. The two most important quantities in this area are the log amplitude intensity  $\chi$  and its variance  $\sigma_\chi^2$ . Experimentally,  $\chi$  values are found by tracking intensity in a subaperture and applying equation (13). The variance then comes from

$$\sigma_\chi^2 = \frac{1}{M} \sum_{m=1}^M (\chi(t_m))^2 - \left( \frac{1}{M} \sum_{m=1}^M \chi(t_m) \right)^2 \quad (32)$$

where  $M$  is again the total number of realizations used from the ensemble and  $\chi(t_m)$  is the log amplitude intensity value at time  $t_m$ .

*3.3.1 Correlation.* The statistical methods used for theoretical structure functions as in Eq. (28) and the validity of averages taken over an entire ensemble of frames require having independent realizations from frame to frame. To study how much one frame is temporally related to another, and thus how well our assumption of having independent frames holds, a correlation coefficient  $\rho$  was found [2]:

$$\rho(n) = \frac{E \left[ \left( I(i) - \overline{I(i)} \right) \left( I(i+n) - \overline{I(i+n)} \right) \right]_i}{\sqrt{E \left[ I^2(i) - \overline{I(i)}^2 \right] E \left[ I^2(i+n) - \overline{I(i+n)}^2 \right]}} \quad (33)$$

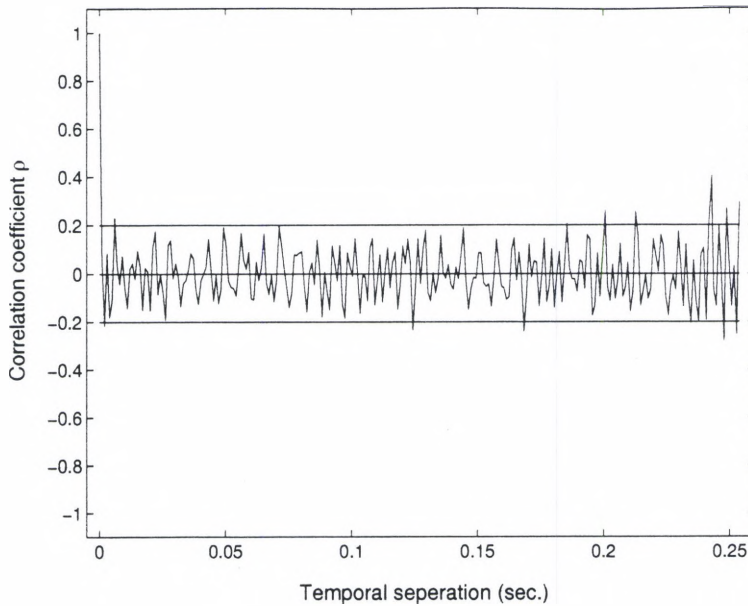


Figure 12. Correlation coefficient  $\rho$  found in laboratory data. Contiguous frames should exhibit independent realizations of the flow.

where  $I(i)$  represents the pixel intensity at time  $i$ , and  $I(i+n)$  represents the intensity at time  $i+n$ . This correlation is a function of frame separation  $n$ . Ideally, this coefficient will show full correlation (a value of one) at no separation and quickly fall to a small value. Figure 12 shows the correlation coefficient for the laboratory data. A threshold of 20% was arbitrarily chosen to illustrate the amount of correlation present. The lab data did indeed quickly become uncorrelated. When studying the experimental data, checking this correlation will determine how many independent frames are available for statistical analysis in a given ensemble of data.

*3.3.2 Intensity Distribution.* The distribution of scintillation intensity values has been theoretically determined by Goodman [11] as a Gaussian distribution,

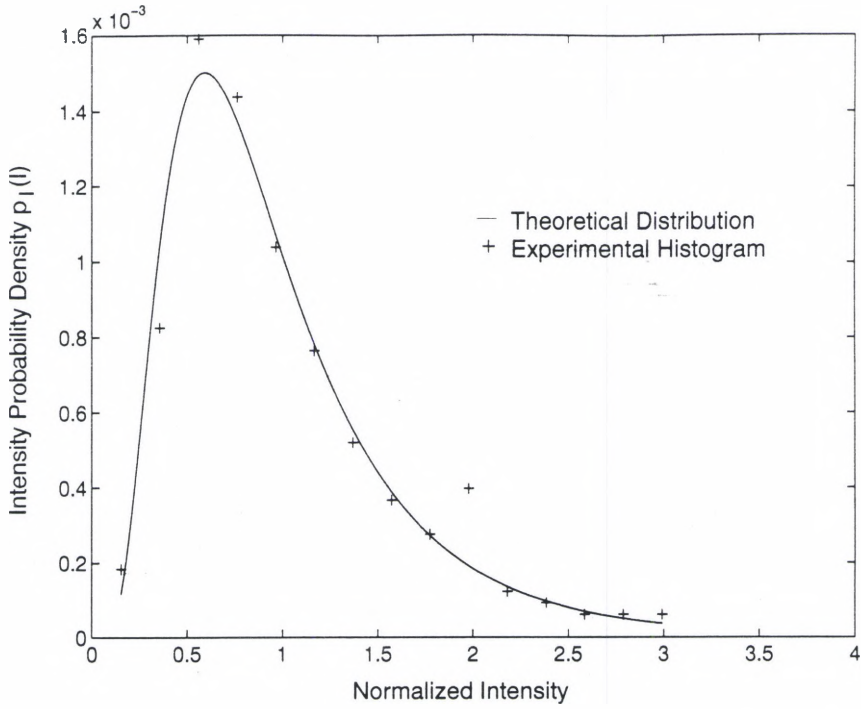


Figure 13. Distribution of intensity probability density acquired from a H-WFS.

and was given earlier as

$$p_I(I) = \frac{1}{2\sqrt{2\pi}\sigma_\chi I} \exp\left\{-\frac{\left(\frac{1}{2} \ln \frac{I}{I_0} - \bar{\chi}\right)^2}{2\sigma_\chi^2}\right\}. \quad (34)$$

Experimentally, this intensity distribution can be found by performing a histogram on the intensity values. Comparison between theory and actual experimental data will quantify the ability of the experimental setup to monitor intensity, and of theory to correctly model the turbulence present. A typical distribution is shown in Fig. 13. This data shows that theory and the experimental setup do match in modeling the scintillation present in the laboratory data.

3.3.3 *Fried Parameter.* To allow for comparison with theory we need to experimentally find the variance of the log-amplitude. This is expressed in [12] as

$$\sigma_{\chi}^2 = 0.307 C_n^2 k^{7/6} z^{11/6} \quad (35)$$

with  $C_n^2$ ,  $k$ , and  $z$  as previously defined. Referring to the definition of the Fried parameter as given in Eq. (5), solving for  $C_n^2$ , and then plugging this into Eq. (35) yields an expression for  $r_o$  in terms of the variance of the log-amplitude:

$$r_o = \left[ 0.0184 \frac{4 \pi^2}{k^{5/6} z^{1/6} \sigma_{\chi}^2} \right]^{3/5} \quad (36)$$

This is the third and final way that the Fried Parameter will be experimentally determined.

## CHAPTER IV

### DATA ANALYSIS AND RESULTS

Using the theoretical and statistical methods discussed in previous chapters, we now turn our attention to characterizing wavefront data taken during the communications experiment in Hawaii. We will attempt to use both phase and intensity tools in this study. The first section will explain the categorization of the data into sets, the second will present results from specific statistical and theoretical methods, the third section will compare data from the two mountain sites, and the final section will summarize the results. All experimental results were determined to an uncertainty of 5 in the last decimal place.

#### *4.1 Data Sets*

The experiment conducted by Wright Laboratories in Hawaii during August and September of 1995 involved the collection of large amounts of H-WFS image data. This data was gathered at a low altitude and over a long horizontal optical path through the earth's atmosphere. Two Hartmann Wave Front Sensors were used,

one on Mount Haleakala and one on Mauna Loa. These setups contained a H-WFS as explained in Chapter III, with optics in front of the sensor to relay the large pupil to the smaller camera pixel array. Figure 4 displayed this setup, which contained the relay optics, the H-WFS, and a line filter that allowed only light at the experimental wavelength through to the camera.

Infrared laser light was emitted from each experimental site, passed over land and water through 150 km of turbulent atmosphere, and was received at the opposite site. Images were taken in sets of 50 or 256 snapshots and then stored to a computer. The camera frame rate was varied between sets to allow for different camera integration times and to capture different time-varying structures. Calibration images as discussed in section 3.1.1 were also taken and stored as separate sets. Each set was assigned a three digit number. Image sets from Mt. Haleakala were numbered 001-241, and from Mauna Loa numbered 500-539. Some sets were combined during analysis to provide larger ensembles. This chapter will focus on presenting results from 12 data sets. These sets are introduced in Table 1. Set 372 contains laboratory data. Data sets whose graphs do not appear in this chapter will have graphs presented in Appendix A.

## 4.2 *Slope Structure Functions*

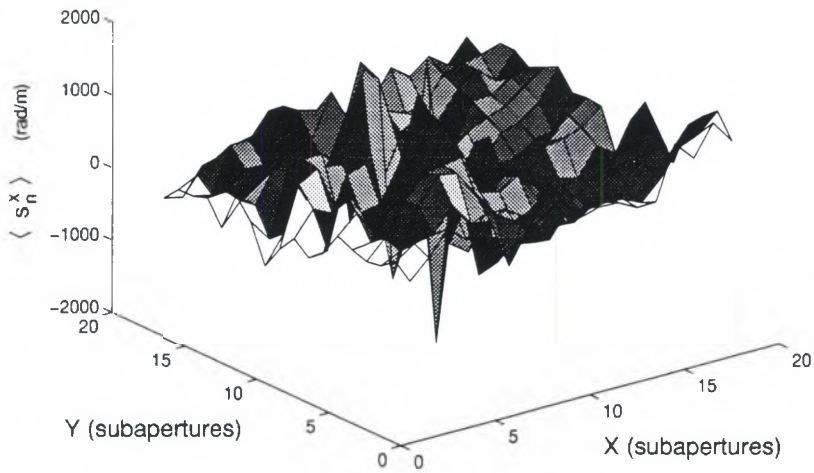
Slope structure functions were found for a number of data sets taken in Hawaii. One of the first steps in studying these functions is the determination of



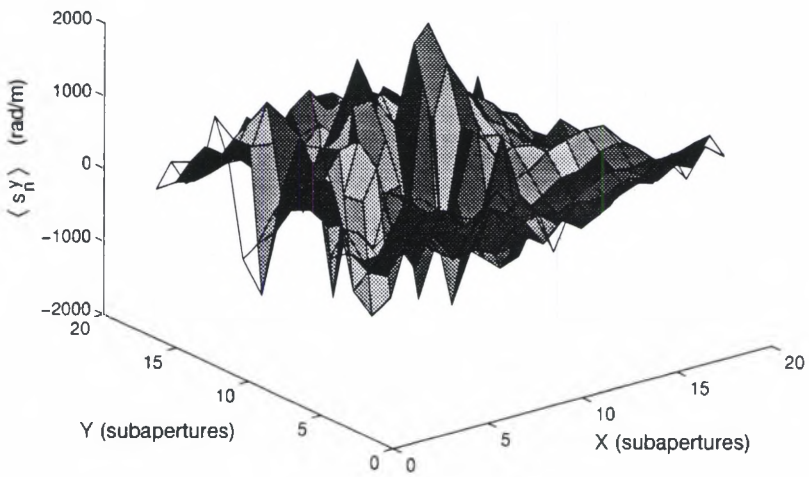
Table 1. Summary of H-WFS image data sets presented.

Data Set	Time Taken	Frame Rate (frames/sec)	# Frames
004	0600	500	256
005	0604	244	256
006	0606	125	256
007	0610	48	256
008	0628	1001	256
009	0633	500	512
015	0033	500	768
024	0046	100	256
507	0210	20	256
523	0730	500	50
524	0740	500	150
372	laboratory	1000	256

homogeneity and isotropy of the slope data. As discussed in Section 3.2.2, this can be accomplished by examining the variance of the slopes. For data set 004 we see in Figs. 14 and 15 that the average slope values  $\langle s_n^x \rangle$  are fairly uniform and small when compared to the variances  $\langle (s_n^x)^2 \rangle$ , but that the slope variances are not very uniform. This implies that the turbulence is not homogeneous, but is not sufficient proof. Figure 16 shows comparison between theoretical and experimental slope structure functions for data set 004, which is used to determine the Fried parameter  $r_o$ . For set 004, we find  $r_o$  values from the slope structure function of around  $0.0025 \pm 0.0005$  m.

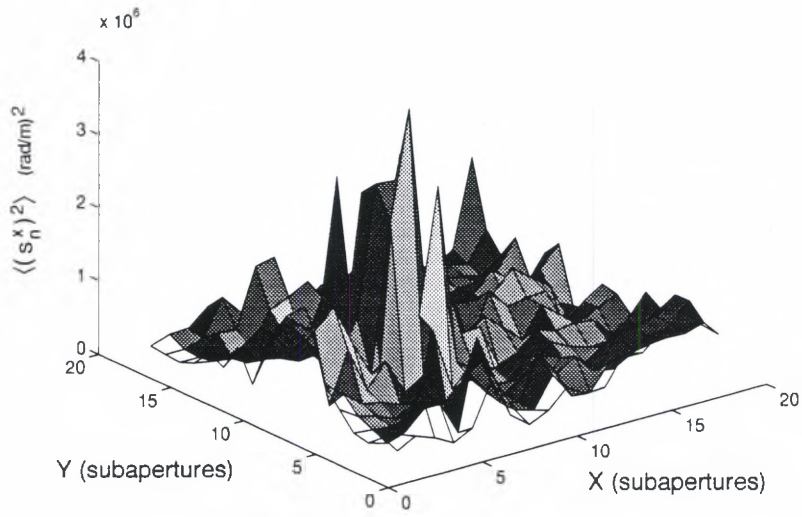


(a)

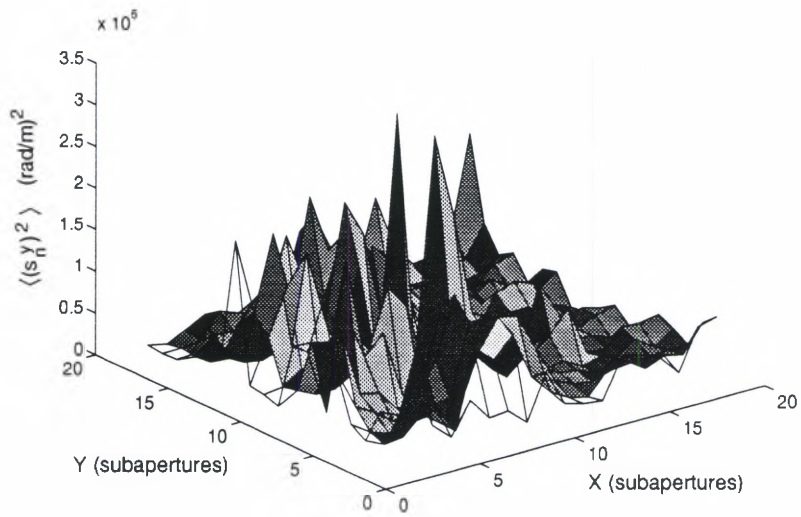


(b)

Figure 14. Average slope values for Data Set 004 (a) X-slope averages; and (b) Y-slope averages across the subaperture.

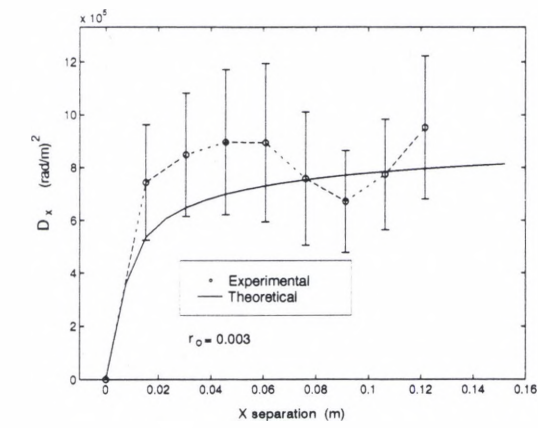


(a)

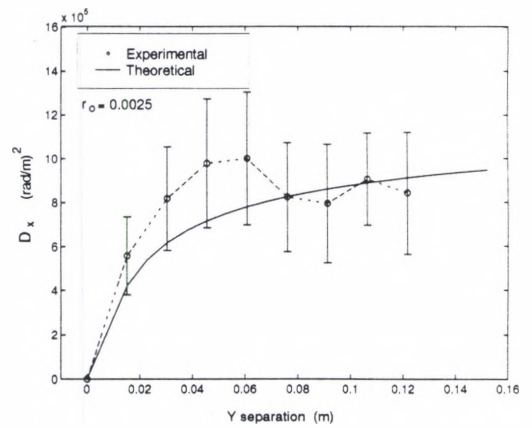


(b)

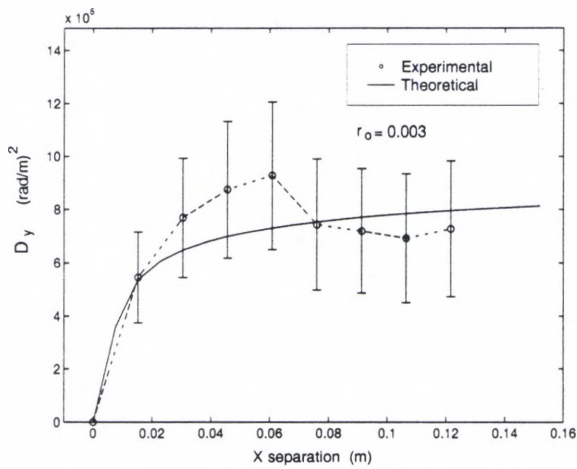
Figure 15. Slope variance values for Data Set 004 (a) X-slope variances; and (b) Y-slope variances across the subaperture.



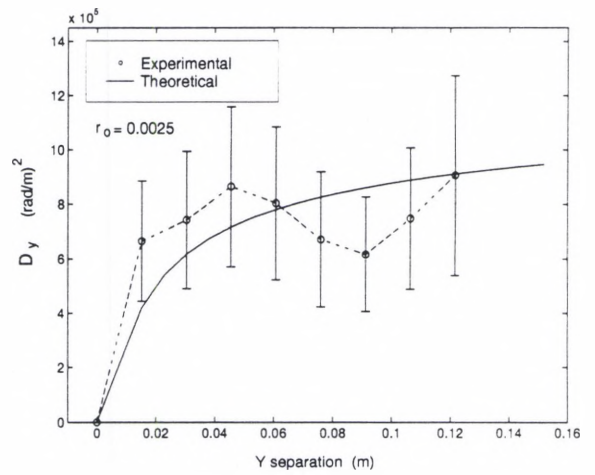
(a)



(b)



(c)



(d)

Figure 16. Self-slope structure functions for experimental data set 004 fitted to theory: (a) X-slopes, x-shifts, (b) X-slopes, y-shifts, (c) Y-slopes, x-shifts, and (d) Y-slopes, y-shifts.

Table 2. Summary of slope-method results from experimental image data sets.

Data Set	$r_o$ : slope variance (m)	$r_o$ : slope structure functions (m)
004	.0039	.0025
005	.0040	.0030
006	.0046	.0030
007	.0053	.0040
008	.0049	.0035
009	.0051	.0035
015	.00276	.0020
024	.003	.0035
507	.006	.015
523	.0036	.020
524	.0051	.015
372	.0332	.030

### 4.3 Site Specifics

Table 2 contains  $r_o$  values for each data set as determined from the variance of the slope values and the structure functions performed on the slopes. These values are very small for the data from Haleakala, on the order of millimeters. For the data taken from Mauna Loa the  $r_o$  values are on the order of centimeters, still small but more in line with traditionally accepted values. Table 3 presents  $r_o$  values based on the scintillation measured, using the variance of the log-amplitude fluctuations  $\sigma_\chi^2$  as explained in Eq. (36).

Looking at the experimental data, we see that these results contain very small values for the Fried parameter based upon slope structure function analysis for the Haleaka data, and small but more traditional values for the Mauna Loa data. Examining the variance of the log-amplitude  $\sigma_\chi^2$ , we see that the approximation of

Table 3. Summary of intensity-method results from experimental image data sets.

Data Set	$r_o$ : scintillation (m)	$\sigma_x^2$	$\bar{\chi}$
004	.4835	.0912	-.1152
005	.2913	.2122	-.2738
006	.2657	.2474	-.2613
007	.3483	.1576	-.1525
008	.446	.1044	-.1164
009	.4058	.1221	-.1274
015	.4397	.1069	-.1116
024	.6866	.0509	-.059
507	.3259	.176	-.165
523	.8286	.0372	-.0448
524	.5593	.0716	-.0749
372	3.408	.00346	-.00346

weak turbulence discussed in Section 2.3 has been violated for the data taken at Mt. Haleakala, and has not been violated for much of the data received at Mauna Loa. Approximations made in theoretically defining the slope structure function may not hold for the data from Haleakala. The  $r_o$  values found as a result of scintillation analysis are on the order of tens of centimeters. These values would imply that the seeing conditions through the given turbulence are good, but again the large intensity variations present mean that the power being delivered to the detector is not steady. Data set 372 contains images from the laboratory. The  $r_o$  values from this data are large, and the scintillation present is noticeably small implying that the lab turbulence used falls well within the weak turbulence regime. The two  $r_o$  values found from the laboratory slope values, one using the slope variance and Eq. (31) and one using the structure functions, match each other very well. As this was the

only data with very small scintillation, it is probable that strong intensity variations affect the applicability of Eq. (31) and bring about the discrepancies found between these two methods in the other data. We also note that the equality between  $\sigma_\chi^2$  and  $\bar{\chi}$  in Eq. 18 does hold for our experimental data. These two values are within 12% of each other on average for this experiment. This leads us to believe that the scintillation theory is doing a valid job in predicting scintillation statistics.

#### 4.4 *Summary*

Twelve H-WFS data sets were analyzed in a variety of ways to characterize the turbulence encountered by optical signals under the given conditions. The majority of data sets resulted in very strong turbulence causing extreme scintillation. Data from the experimental receiver site at Mauna Loa yielded  $r_o$  values from slope structure function analysis that were an order of magnitude larger than data from the Haleakala site. The Mauna Loa site also had noticeably smaller  $\sigma_\chi^2$  values meaning the scintillation at the Mauna Loa receiver was less than the scintillation encountered at Heleakala. These results indicate that the turbulence was stronger near the Mauna Loa site, and thus an optical path leaving Mauna Loa would have its field strongly perturbed early on. This would cause more interference later in the optical path and thus more scintillation. Light leaving Haleakala seemed to encounter its strongest turbulence close to the receiver at Mauna Loa, and thus less time and distance was present in which scintillation could occur. These statistics seem to indicate that much care needs to be given in determining the placement

of optical communications and other free-space laser sites, due in large part to the scintillation that could result.

One likely reason for the results found is that the experimental site at Mauna Loa was farther from the shoreline and thus light had to pass over a larger amount of land at this end of the optical path. Land causes much stronger temperature gradients than bodies of water, due in large part to the greater amount of absorption of the sun's energy by earth during daylight hours.



## CHAPTER V

### CONCLUSIONS

This chapter highlights the major results and conclusions of this work. Recommendations for related future work are also discussed.

#### *5.1 Results and conclusions*

A variety of methods have been presented to achieve the characterization of atmospheric turbulence using a Hartmann Wavefront Sensor. The H-WFS is a good tool for this characterization. The determination of the atmospheric Fried parameter has been achieved with both phase and intensity statistics through the use of H-WFS camera images. The amount of scintillation present in the conditions studied means that low altitude long horizontal paths present problems in the area of the delivery of power from a laser. The Rytov approximation used in the theory applying to weak turbulence breaks down under the studied conditions. An attempt to correct wavefront distortions through the use of adaptive optics at the receiver will not fix the intensity variation problems present under these conditions. Strong

phase variations are also present. Extreme care is necessary in choosing ground-based sites for free-space laser applications. The Hartmann WFS has shown itself to be versatile enough to characterize turbulence under different conditions and provide information for this decision.

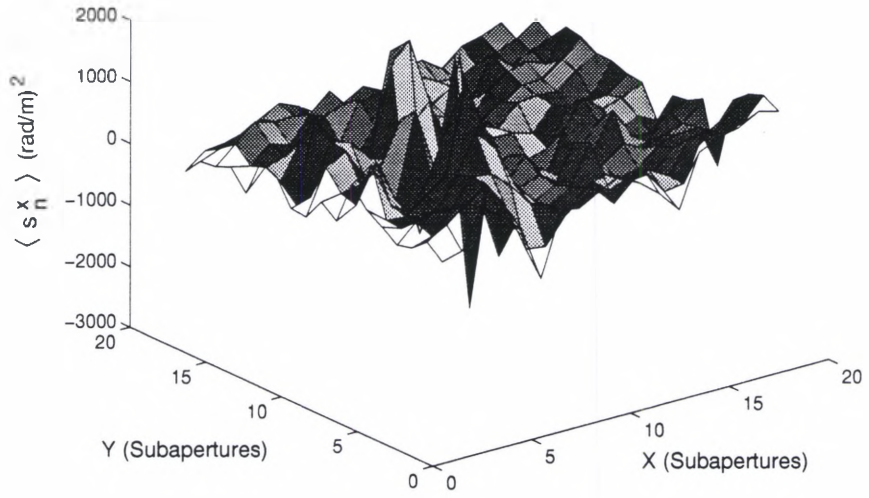
## *5.2 Further Study*

Issues that must now be investigated include studying optical paths that contain a mix of both low and high-altitude propagation. The spatial statistics of scintillation parameters is another issue that may aid in the understanding of effects scintillation may cause. The placement of communications equipment with respect to land masses appears to be a major factor, and should be taken into account when further research sites are chosen.

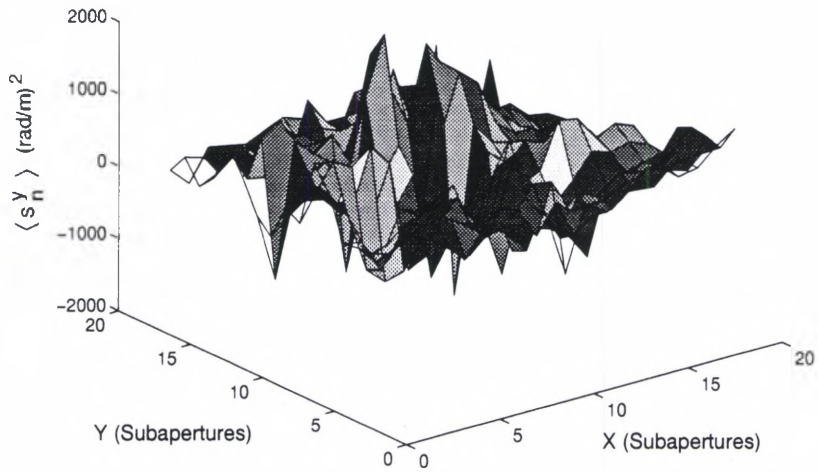
## *APPENDIX A*

### DATA SET IMAGES

The data taken in the Optical Communications experiment in Hawaii yielded a large amount of data. A portion of this data was examined for this work. Plots showing tests for homogeneity using slope averages and variances are shown for some of this data, as well as plots showing the comparison with slope structure function theory. The intensity probability distribution for a data set from Mauna Loa is also included to show the match between theory and experiment for measured intensity values. Only structure function plots are shown for the remaining data.

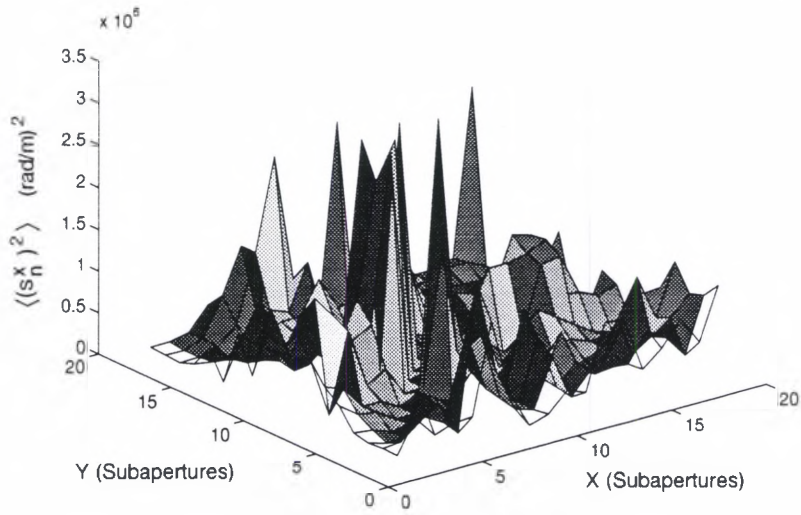


(a)

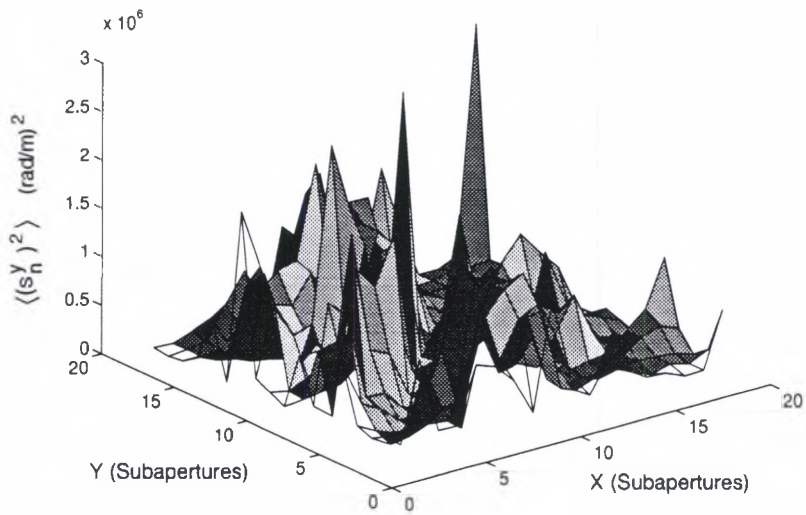


(b)

Figure 17. Average slope values for Data Set 005 (a) X-slope averages; and (b) Y-slope averages across the subaperture.

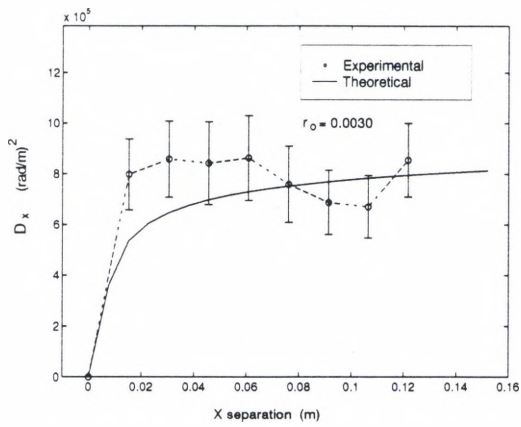


(a)

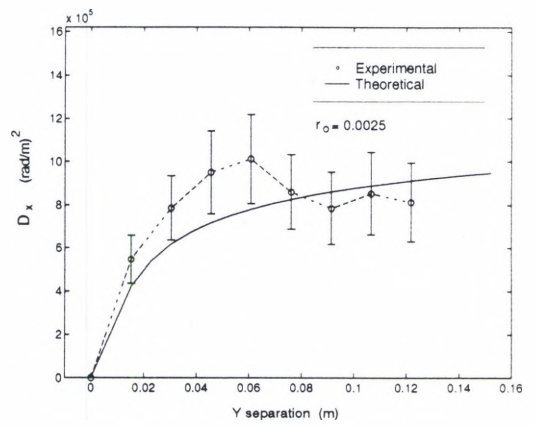


(b)

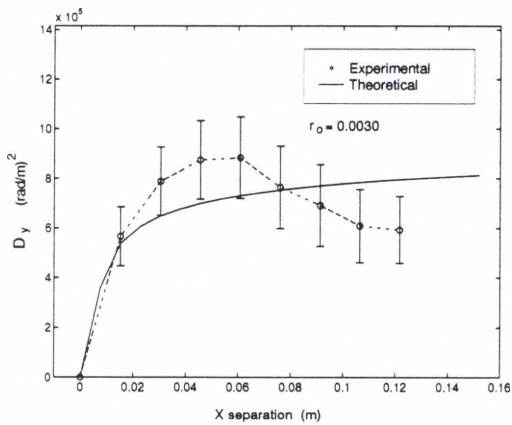
Figure 18. Slope variance values for Data Set 005 (a) X-slope variances; and (b) Y-slope variances across the subaperture.



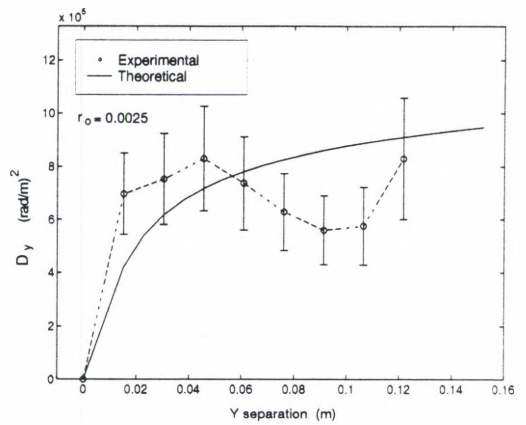
(a)



(b)



(c)



(d)

Figure 19. Self-slope structure functions for experimental data set 005 fitted to theory: (a) X-slopes, x-shifts, (b) X-slopes, y-shifts, (c) Y-slopes, x-shifts, and (d) Y-slopes, y-shifts.

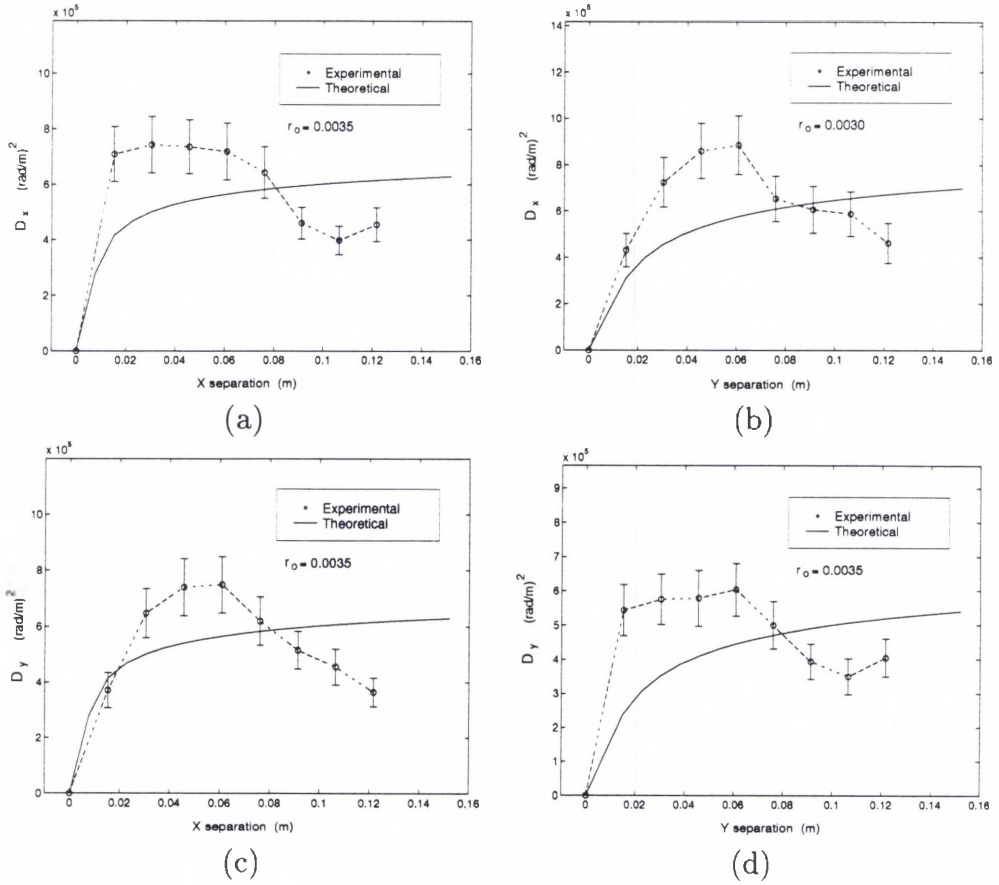


Figure 20. Self-slope structure functions for experimental data set 008 fitted to theory: (a) X-slopes, x-shifts, (b) X-slopes, y-shifts, (c) Y-slopes, x-shifts, and (d) Y-slopes, y-shifts.

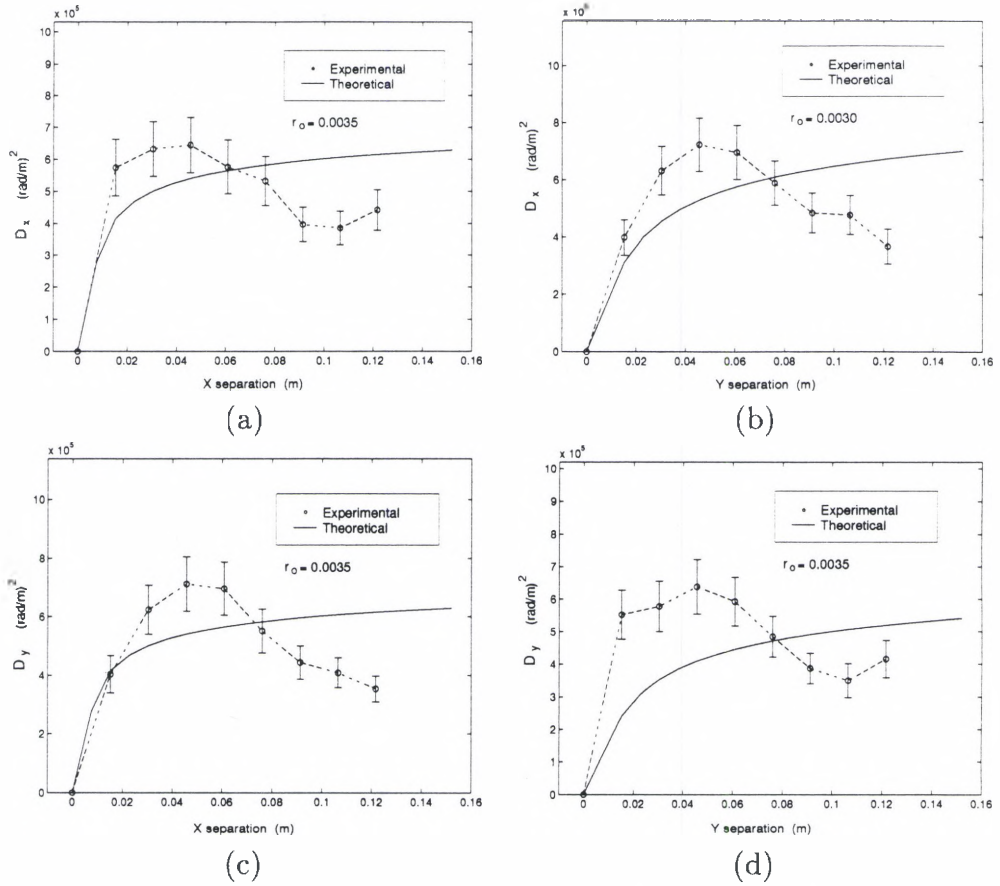
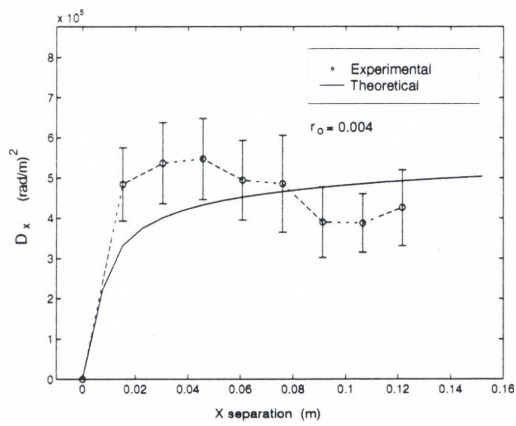
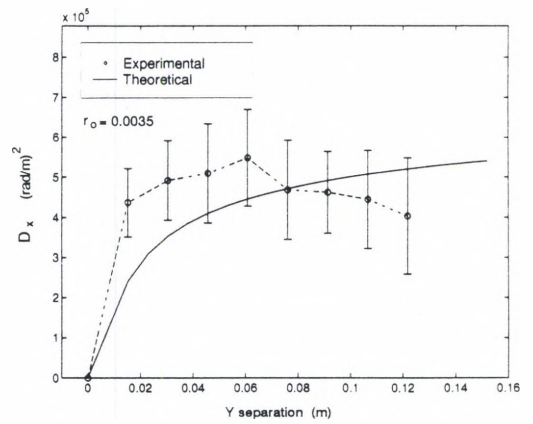


Figure 21. Self-slope structure functions for experimental data set 009 fitted to theory: (a) X-slopes, x-shifts, (b) X-slopes, y-shifts, (c) Y-slopes, x-shifts, and (d) Y-slopes, y-shifts.

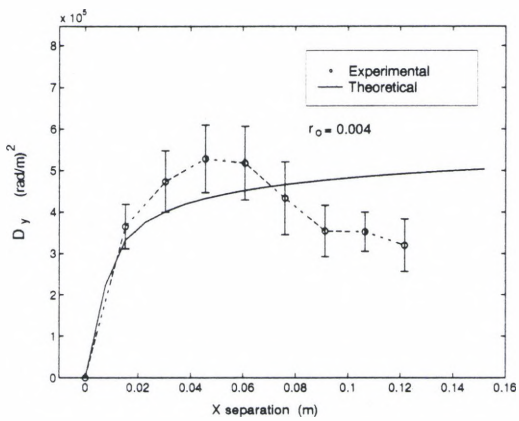




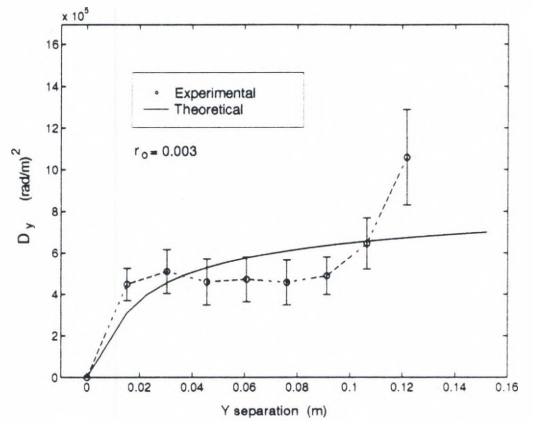
(a)



(b)



(c)



(d)

Figure 22. Self-slope structure functions for experimental data set 024 fitted to theory: (a) X-slopes, x-shifts, (b) X-slopes, y-shifts, (c) Y-slopes, x-shifts, and (d) Y-slopes, y-shifts.

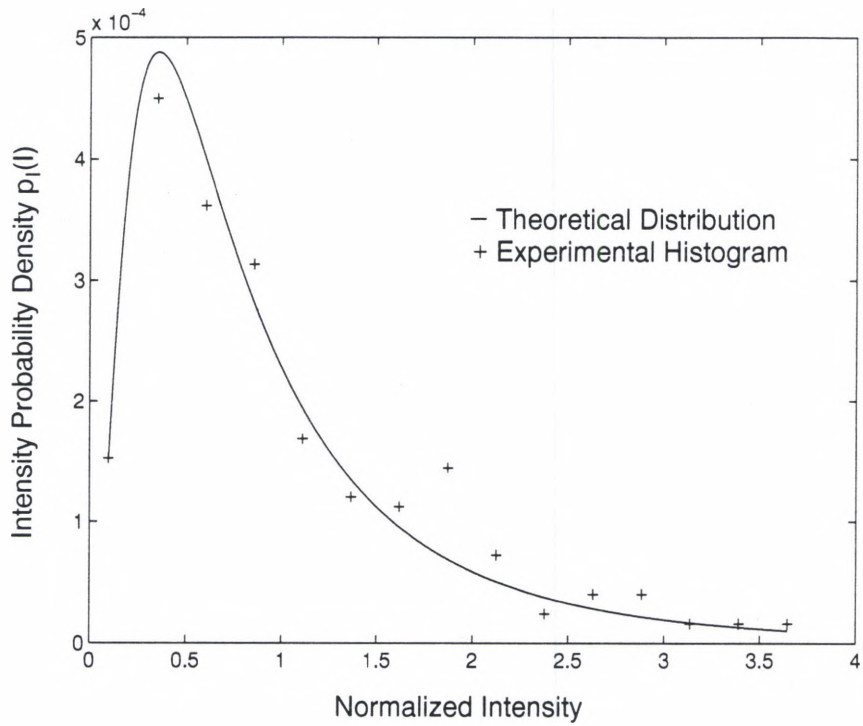
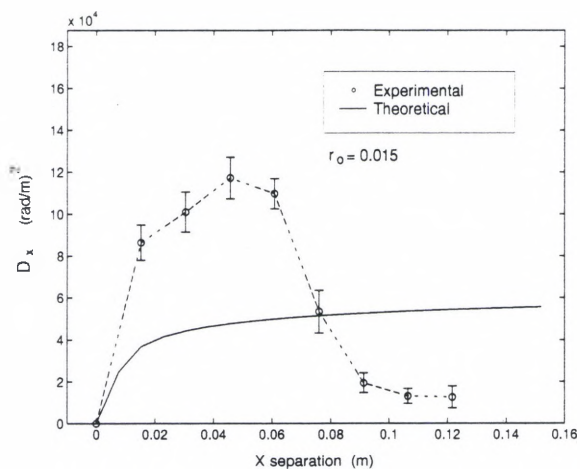
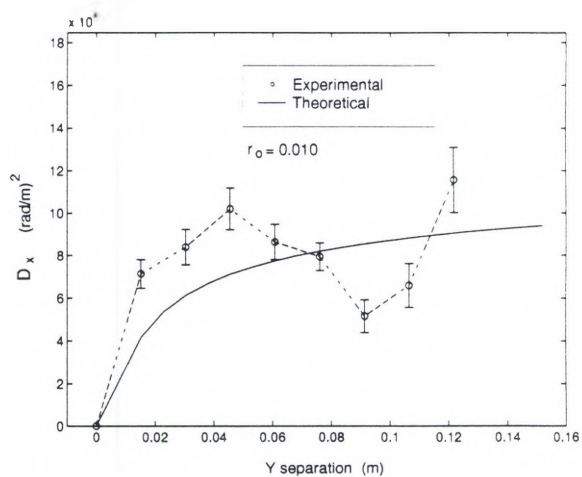


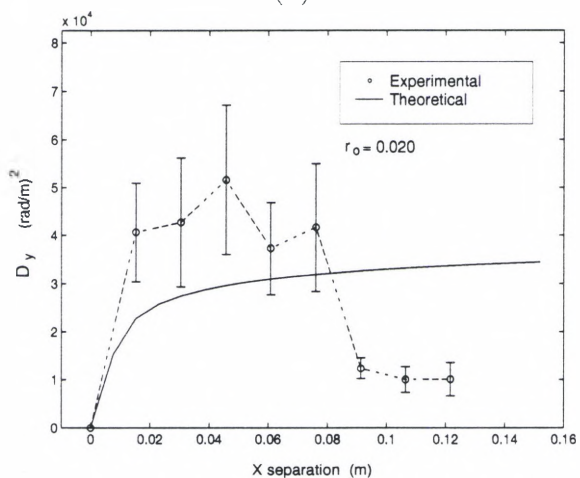
Figure 23. Intensity Probability density for data set 507.



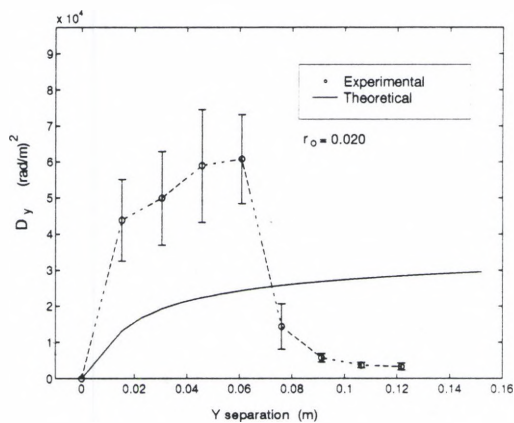
(a)



(b)

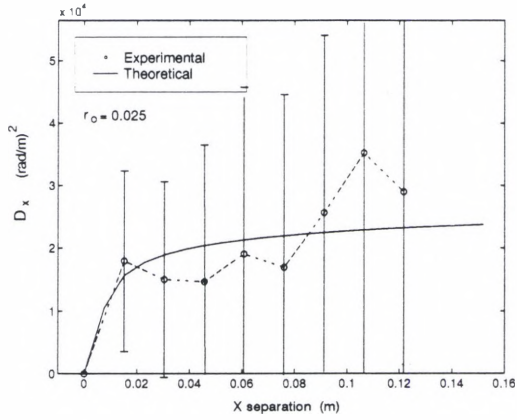


(c)

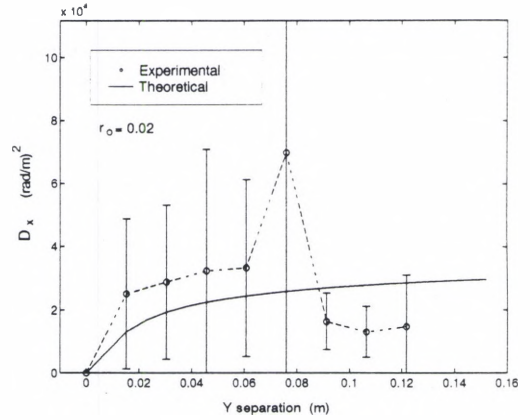


(d)

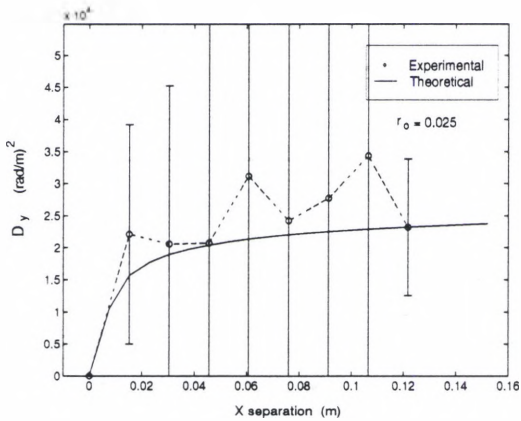
Figure 24. Self-slope structure functions for experimental data set 507 fitted to theory: (a) X-slopes, x-shifts, (b) X-slopes, y-shifts, (c) Y-slopes, x-shifts, and (d) Y-slopes, y-shifts.



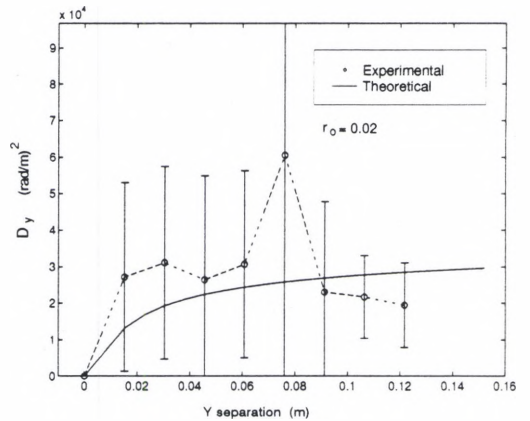
(a)



(b)

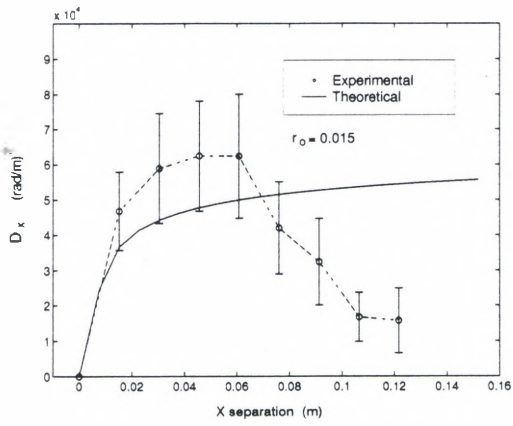


(c)

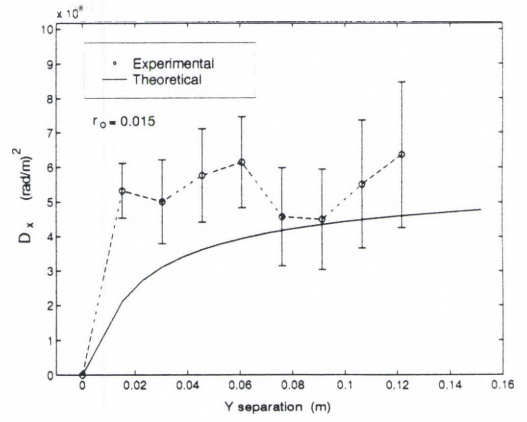


(d)

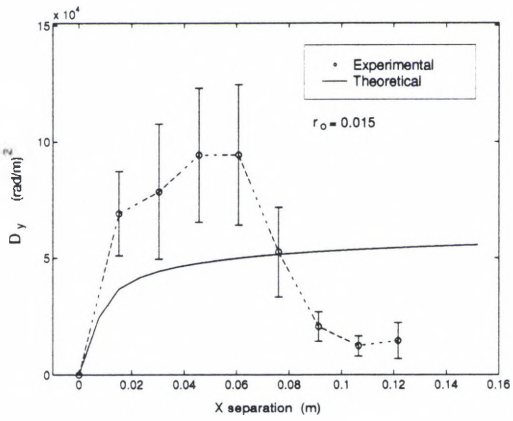
Figure 25. Self-slope structure functions for experimental data set 523 fitted to theory: (a) X-slopes, x-shifts, (b) X-slopes, y-shifts, (c) Y-slopes, x-shifts, and (d) Y-slopes, y-shifts.



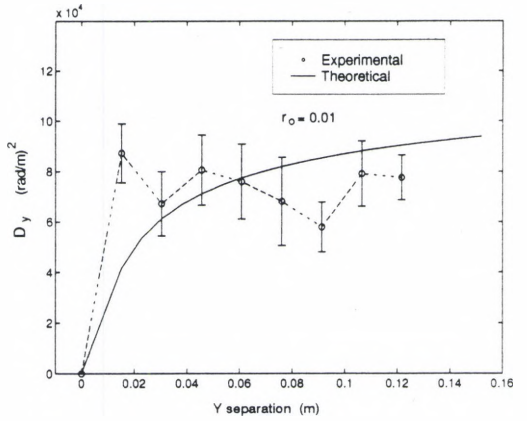
(a)



(b)



(c)



(d)

Figure 26. Self-slope structure functions for experimental data set 524 fitted to theory: (a) X-slopes, x-shifts, (b) X-slopes, y-shifts, (c) Y-slopes, x-shifts, and (d) Y-slopes, y-shifts.

## *APPENDIX B*

### COMPUTER CODE GUIDE

This appendix is intended to provide a short overview of the computer code developed to analyze H-WFS images. A brief description of each program or module is presented. All code was written for use in the MATLAB environment. This code includes functions and scripts called from the MATLAB command line with the proper parameters. Detailed comments discussing the exact input and output parameters are found in comment form in the MATLAB M-files themselves. Functions inherent to MATLAB itself are documented and may be accessed by typing `help function` at the command line, where `function` is the name of the function in question.

#### *B.1 Slope Determination*

*B.1.1 ACENTRAVG.M.* Uses Hartmann Wave Front Sensor images to find average centroid locations of the focused spots in each subaperture. These centroids are used later to center each subaperture on the spot within it. Uses `at1cc3gb.m` file. Saves centroid locations to a file for use in `afslope.m`.

*B.1.2 ATLCC3GB.M.* Program used to calibrate H-WFS images and determine spot location in each subaperture.

*B.1.3 AFSLOPES.M.* Uses H-WFS images and the averaged spot locations to find slope values for each subaperture in the pupil. Uses `atlcc4.m`. Saves slopes and a mask representing valid subaperutures to files on disk.

*B.1.4 ATLCC4.M.* Program used to calibrate H-WFS images and determine slope values for an individual image. Also determines validity of the images being used. Uses `peakfnd3.m`

*B.1.5 PEAKFND3.M.* Function written by Tim Pennington and edited by Wesley Bernard to determine, to sub-pixel accuracy, the location of a peak (focused spot). Compared to centroid method to determine validity of a spot.

*B.1.6 SANALYZE3.M.* Program used to calibrate H-WFS images, determine slope values, and reconstruct a phase screen for each image. Uses `r15.mat` or a similar data file. Saves phase screens to files for future viewing.

*B.1.7 R15.MAT.* Matlab data file containing reconstruction matrix. Used by `sanalyze3.m` to reconstruct slope values into a phase screen. Results from a FORTRAN file, and is based upon specific physical parameters.

*B.1.8 VIEWER.M.* Views an individual phase screen created by `sanalyze3.m`.

*B.1.9 VMOVIE2.M.* Views a collection of phase screens in a movie format.

## *B.2 Statistical Analysis Using Slope Values*

*B.2.1 DSGEN.M.* Computes the normalized theoretical slope structure function for  $x$ ,  $y$ , and  $45^\circ$  separations. The structure functions are returned as vectors. Uses the `dsxx.m` function.

*B.2.2 DSXX.M.* Computes a value of the theoretical slope structure function. The input parameters are the  $x$  and  $y$  subaperture separations,  $r_o$ , and the subaperture size  $d$ . Returns a single value. Uses the `ds_arg` function.

*B.2.3 DS\_ARG.M.* Evaluates the normalized integrals for the theoretical slope structure function.

*B.2.4 ACEFILES.M.* Reads the H-WFS slope filenames from a directory. The full pathname must be provided. Only H-WFS slope files must be in the given directory or the function will abort. The file names are returned in the rows of a matrix.

*B.2.5 ACEREAD.M.* Reads an H-WFS slope file and returns the  $x$  slope,  $y$  slope, amplitude, and mask matrices. The full path must be specified.

*B.2.6 ACEVIEW.M.* Displays a matrix using the ‘hot’ colormap. Useful for debugging.



*B.2.7 DSX.M.* Computes structure functions for the  $x$  separations. Inputs are a mask matrix and two slope matrices. Outputs a structure function and mask matrix.

*B.2.8 DSY.M.* Computes structure functions for the  $y$  separations. Inputs are a mask matrix and two slope matrices. Outputs a structure function and mask matrix.

*B.2.9 DSN45.M.* Computes structure functions for the  $-45^\circ$  separations. Inputs are a mask matrix and two slope matrices. Outputs a structure function and mask matrix.

*B.2.10 DSP45.M.* Computes structure functions for the  $+45^\circ$  separations. Inputs are a mask matrix and two slope matrices. Outputs a structure function and mask matrix.

*B.2.11 DSTRUCT.M.* A script which computes the structure functions for all slope and separation combinations. Accumulates running sums of the structure function, squared structure function, and mask matrices. These sums are used to compute the structure function, structure function variance, and sum matrices. Inputs are a string containing the path to the directory containing the H-WFS slope files.

*B.2.12 DSTAR.M.* Removes the average slopes and computes the structure functions for all slope and separation combinations. Accumulates running sums of the structure function, squared structure function, and mask matrices. These sums are used to compute the structure function, structure function variance, and sum matrices. Inputs are a string containing the path to the directory containing the H-WFS slope files.

*B.2.13 WFS\_STAT.M.* Computes the slope average, variance, and sum at each point in the aperture. Writes the results to `.mat` files. Inputs are a string containing the path to the directory containing the H-WFS slope files.

*B.2.14 DVIEW.M.* Displays the submatrices of a structure function matrix in increasing subaperture separation. Inputs are a structure function matrix. Useful for debugging.

*B.2.15 DPICK.M.* Picks the structure function values corresponding to a particular anchor point and returns those values in a column. Inputs are a set of vectors listing the x-y coordinates of the structure function and a structure function matrix.

*B.2.16 SPCAVG.M.* Spatially averages the structure function and computes confidence intervals. Inputs are a set of vectors listing the x-y locations to be averaged; and the structure function, variance, and sum matrices. Outputs are two

vectors; one containing the spatially averaged structure function, the other containing the corresponding confidence intervals.

*B.2.17 CORRI2.M.* Uses intensity information to determine the correlation function  $\rho$  at different subaperture locations. Saves data to the `corr.mat` file.

*B.2.18 CORRVIEW.M.* Takes an input of a subaperture location, and picks out valid  $\rho$  values from `corr.mat` to give a graph of the correlation function.

*B.2.19 FITAB.M.* Fits the spatially averaged experimental structure function with theory for the A slopes for separations in the B direction. Inputs are the number identifying the data set to be studied, the minimum and maximum separation values B may take, and the step value to use in incrementing through the separations. This yields a value for the Fried Parameter  $r_o$  based upon slope structure functions. Uses `sfgenab.m`.

*B.2.20 SFGENAB.M.* Creates a theoretical slope structure function for slopes in direction A for shifts in direction B. Uses an input value for  $r_o$ .

*B.2.21 HISTT.M.* Takes log-amplitude information from the slope data files and performs a histogram to examine the values of  $\chi$ .

*B.2.22 PROBI4.M.* Takes field amplitude information from slope data files and creates an experimental probability distribution for normalized intensity values.

*B.2.23 PLOTONEB.M.* Plots structure functions for all valid anchor points. Uses the `sfaavgxsub.m` and `sfaavgysub.m` functions. Inputs are the number identifying the data set to be studied and which of the 4 slope direction-shift direction pairs to view.

*B.2.24 SFAVGXSUB.M.* Uses the `dpick.m` function to pick the structure function values for each anchor point in the aperture.

*B.2.25 SFPLOTSUB.M.* Plots structure functions in which all valid anchor points that have the same number of allowable shifts in a given direction have been averaged together. Uses the `sfaavgxsub.m` and `sfaavgysub.m` functions. Inputs are the number identifying the data set to be studied and whether or not to compute confidence intervals for each structure function data point. All four of slope direction-shift direction pairs are plotted on the same graph.

*B.2.26 PLOTONE.M.* Plots the same values as `sfplotsub.m`, but only plots one of the four slope direction-shift direction pairs. Which of the four to view is an additional input.

*B.2.27 SFPLOT.M.* Plots structure functions in which all valid anchor points in the pupil have been averaged together. All four slope direction-shift di-

rection pairs are plotted on the same graph. Uses the `sfavgx.m` and `sfavgy.m` functions. Inputs are the number identifying the data set to be studied and whether or not to compute confidence intervals for each structure function data point.

*B.2.28 SFAVGX.M.* Uses the `spcavg.m` function to pick out and average the structure functions for each shift size.

*B.2.29 AVGNAN2.M.* Takes an input array and averages into a vector (similar to the Matlab `avg` function) disregarding NaN values.

*B.2.30 AVGNAN.M.* Takes an input array and averages into a single number (similar to the Matlab `avg(avg())` function) disregarding NaN values.

*B.2.31 AVGINF.M.* Takes an input array and averages into a single number disregarding Inf values.

*B.2.32 MINNAN/MAXNAN.M.* Takes an array and finds the minimum/maximum value disregarding NaN values.

## BIBLIOGRAPHY

1. I. Newton, "Optics," in *Great Books of the Western World* (R. M. Hutchins, ed.), vol. 34, Chicago: Encyclopedia of Britannica, 1952.
2. M. C. Roggemann and B. M. Welsh, *Imaging Through Turbulence*. Boca Raton, Florida: CRC Press, 1996.
3. D. E. Spreen and C. B. Hogge, "Characterizing high-altitude horizontal path optical propagation," in *SPIE Proceedings on Laser Beam Propagation And Control* (H. Weichel and L. F. DeSandre, eds.), vol. 2120, pp. 2–9, 1994.
4. R. J. Feldmann, "Airborne laser communications scintillation measurements," Master's thesis, Graduate School of Engineering, Air Force Institute of Technology (AETC), Wright-Patterson AFB OH, 1987.
5. C. E. E. Silbaugh, "Characterization of atmospheric turbulence over long horizontal paths using optical slope measurements," Master's thesis, Graduate School of Engineering, Air Force Institute of Technology (AETC), Wright-Patterson AFB OH, 1995.
6. L. D. Weaver and R. Butts, "Ablex: High altitude laser propagation experiment," in *SPIE Proceedings on Laser Beam Propagation And Control* (H. Weichel and L. F. DeSandre, eds.), vol. 2120, pp. 30–42, 1994.
7. E. P. Magee and B. M. Welsh, "Characterization of laboratory generated turbulence by optical phase measurements," *Optical Engineering*, pp. 3810–3817, Nov. 1994.
8. D. L. Fried, "Optical resolution through a randomly inhomogeneous medium for very long and very short exposures," *Journal of the Optical Society of America*, vol. 56, pp. 1372–1379, 1966.
9. M. C. Roggemann, B. M. Welsh, P. J. Gardner, R. L. Johnson, and B. L. Pederesen, "Sensing three-dimensional index-of-refraction variations by means of optical wavefront sensor measurements and tomographic reconstruction," *Optical Eng*, vol. 34, pp. 1374–1384, May 1995.
10. A. Kolmogorov, *Turbulence, Classical Papers on Statistical Theory*. New York: Wiley-Interscience, 1961.
11. J. W. Goodman, *Statistical Optics*. New York: Wiley, 1985.

12. W. L. Wolfe and G. J. Zissis, *The Infrared Handbook*. Washington D.C.: Office of Naval Research, Dept. of the Navy, 1978.
13. V. I. Tatarski, *Wave Propagation in a Turbulent Medium*. New York: Dover Publications, 1967.
14. C. Roddier and F. Roddier, "Correlation measurements on the complex amplitude of stellar plane waves perturbed by atmospheric turbulence," *Journal of the Optical Society of America*, vol. 63, pp. 661-663, June 1973.
15. F. D. Eaton, W. A. Peterson, and J. R. Hines, "Phase structure function measurements with multiple apertures," in *SPIE Proceedings on Propagation Engineering*, vol. 1115, pp. 218-223, 1989.
16. M. C. Roggemann, P. J. Gardner, B. M. Welsh, R. D. W. Bowersox, and D. W. Jewell, "Gas flow visualization by means of sheared beam interferometry: sensitivity, dynamic range, and integrated density estimation," *Measurement*, September 1995. Accepted for publication.
17. T. L. Pennington, "Performance comparison of the shearing interferometer and hartmann wavefront sensors," Master's thesis, Graduate School of Engineering, Air Force Institute of Technology (AETC), Wright-Patterson AFB OH, 1993.
18. E. P. Wallner, "Optimal wave front correction using slope measurements," *Journal of the Optical Society of America*, vol. 73, pp. 1771-1776, 1983.
19. E. E. Silbaugh, B. M. Welsh, and M. C. Roggemann, "Characterization of atmospheric turbulence over long horizontal paths using optical slope measurements," in *SPIE proceedings on Image Propagation Through the Atmosphere*, vol. 2828, August 1996.
20. D. L. Snyder *et al.*, "Image recovery from data acquired with a charge-coupled-device camera," *Journal of the Optical Society of America*, vol. 10, pp. 1014-1023, May 1993.
21. M. C. Roggemann, "Optimal performance of fully and partially compensated adaptive optics systems using least-squares and minimum variance phase reconstruction," *Computational Electronics Engineering*, vol. 18, pp. 451-466, 1992.
22. A. Papoulis, *Probability, Random Variables, and Stochastic Processes* (3rd edition). New York: McGraw Hill, Inc., 1991.
23. P. J. Gardner, M. C. Roggemann, and B. M. Welsh, "Quantification of frozen flow properties for a turbulent mixing layer of Helium and Nitrogen gas," in *SPIE proceedings on Image Propagation Through the Atmosphere*, vol. 2828, August 1996.

## VITA

Wesley Allan Bernard was born in Washington Court House, Ohio in November of 1971. He graduated from Miami Trace High School in 1990, and went on to receive a Bachelor of Science in Physics from Miami University in Oxford Ohio in 1994. Wesley was then accepted into the Graduate Engineering program at the University of Dayton in Dayton, Ohio.

While at the University of Dayton Wesley instructed an undergraduate Physics Lab class, teaching a wide variety of physics topics. He then received an AFOSR/RDL Summer Graduate Student Fellowship to study atmospheric turbulence at Wright Patterson Air Force Base. Wesley then received a GAANN Fellowship to conduct his thesis work.

Mr. Bernard graduated from the University of Dayton in August, 1996 with a Master of Science in Electro-Optic Engineering. He is a member of SPS, SPIE and OSA. He presented a paper dealing with optical propagation along vertical paths at the SPIE Technical Conference 2828 in Denver in August of 1996.

Permanent address: 3512 Bush Rd. NW  
Washington CH, OH 43160